

NANO-RODS $\text{WO}_{3-\delta}$ FOR ELECTROCHROMIC SMART WINDOWS APPLICATIONS

BY

PRAISE SIBUYI

Submitted for partial fulfillment of the requirements for the degree

MAGISTER SCIENTIAE



Promoter: Dr. M. Maaza

Co-Promoter: Prof. D. Knoesen

JUNE 2006
CAPE TOWN



Declaration

I declare that Nano-rods $\text{WO}_{3-\delta}$ for Electrochromic Smart Windows Applications is my own work, that it has not been submitted before for any degree or assessment in any other University, that all the sources I have used or quoted have been indicated and acknowledged by means of complete references

.....
Signature

.....
Date

Acknowledgments

Firstly and foremost, praise and thanks goes to the Almighty God, for His love and Blessings all the time. I would like to thank my supervisors: Dr. Malik Maaza, for his guidance, encouragement, and patience because if it was not for him, the content of this joint work wouldn't have been realized. Prof Dirk Knoesen, who looked closely at the final version of the thesis for English style and grammar, correcting both and offering suggestions for improvement.

To Dr. Terrence Marais, I know you loved to see the end of my work; thanks for the opportunity and warm welcome at Cape Town, rest in peace. I want to further thank all the staff members in the physics department for their support and patience.

I would like to extend my deep appreciation to iTHEMBA LABS for granting me an opportunity to work in such a conducive environment, particularly the Material Research Group. Lisa Godana, thank you for all the administrative support and the warm welcome at the lab, you were like a sister all the time. To Audrey Sauls at Ithemba Labs library, thanks to all your effort in making sure that I get the articles in time, I appreciate your effort and time.

To Dr Chris Theron thanks for listening to all my requests and the assistance with the Evaporator machine. I want to express my gratitude, to Lawrence Ashworths, Karl Springhorn, to mention a few for their technical support in the solid state lab and Remy Bucher in the X-ray diffraction machine. It was a great pleasure sharing an office with Thembi Mhlungu, Noluthando Ntshangase, Maria Modise, and Nonhlanhla Mokoena, thanks guys for all the jokes, I will miss the year 2005.

To my brother Jerry K. Sibuyi, I single you out, for your support, and being there all the time to answer my call and act to my requests. I appreciate every little thing you have done for me. Thanks N'wana mhaki. I believe I owe my deepest thanks to all my family members for their continued support given to me and their undying love. Ndza mi rhandza hikwenu.

I cannot forget to mention, my friends, Fortress Netili, Thulani Hlatswayo, Gaopalelwe (GP) Santswere, for our continuous social gathering at CTICC (nickname), hey guys I'll miss this times and many other close friends that could not fit in this piece of paper, that were with me during the hours of loneliness and desperation. Friends that made it possible that I felt home away from home, I extended my deepest appreciation. Ncebakazi it was nice meeting you. Thanks for the continuous visit and ideas sharing!

It would, of course, be completely amiss for me to end my acknowledgements without recognizing my Palesa, thanks for being nano-meters away from my heart; for your encouragement and understanding my busy schedule. You always made my spare time worth while. Through the wonders of internet and email, I received invaluable references from around the world, and such information has been helpful to the completion of this work. I will send a special word of thank to Prof Claes G. Graqvist (Sweden) for his articles, they have made a meaningful contribution in my work.

I am indebted to the NRF for generously funding my research and offering me the opportunity to expand my cultural and social horizons.



I dedicate this thesis to my parents for their undying love, support and trust.

Abstract

Tungsten oxide is a good electrochromic material which has been used in the construction of smart windows through visible modulation. These smart materials can reversibly change their optical properties with the application of an external voltage. Their ability to lighten and darken on command is ideally suited for energy-efficiency windows. The process itself or the overall reaction should respond in seconds and as quick as possible. First generation electrochromic devices based on cathodic WO_3 in a laminated design employing a polymeric electrolyte have been produced and studied extensively.

Now, Tungsten oxide as a major component in this technology has to be re-engineered to enhance the dynamics of its optical modulation: porous nano-scaled WO_3 with high shape anisotropy such as nanorods are potential candidates. In this work the tungsten oxide nanorods are being synthesized by a thermal evaporation technique and further investigated. The nanorods have been successfully grown on planar substrate of Si(001), Mica and Corning glass at the temperature of about 850°C . High resolution Scanning Electron Microscopy has been used as a primary characterization tool to study their growth. The optical and electrochromic properties were studied in detail by UV-VIS-NIR spectroscopy and cyclic voltametry. The properties of deposited WO_3 nanorods are presented comparing it with the reported results for a standard electrochromic material.

Contents

CHAPTER ONE

1. Introduction and aim of the research project..... 2
2. Why a nano-rod type architecture?..... 9

CHAPTER TWO

- 2.1 Electrochromism in WO_3 11
- 2.2 Origin of electrochromism in WO_3 12

CHAPTER THREE

- 3.1 Structural properties and phase transitions of bulk WO_3 18
 - 3.1.1 Monoclinic phase..... 25
 - 3.1.2 Orthorhombic phase..... 26
 - 3.1.3 Tetragonal phase..... 27
 - 3.1.4 Hexagonal phase..... 28
- 3.2 Optical properties of bulk WO_3 30
 - 3.2.1 UV-VIS spectral range..... 30
 - 3.2.2 Infrared spectral range..... 31
- 3.3 Electronic properties of bulk WO_3 32

CHAPTER FOUR

- 4.1 Literature survey of $\text{WO}_{3-\delta}$ nanorods synthesis..... 38
 - 4.1.1 Atomic force microscopy-like approach..... 38
 - 4.1.2 Thermal evaporation..... 38
 - 4.1.3 Template methodology..... 39
 - 4.1.4 Sputtering..... 39
 - 4.1.5 Thermal assisted spray..... 40
 - 4.1.6 Direct powder heating..... 41
 - 4.1.7 Vapor transport method..... 41

CHAPTER FIVE

5. Growth mechanisms.....	42
5.1 Standard growth models.....	42
5.2 Vapor-Liquid-Solid (VLS) growth mode.....	46

CHAPTER SIX

6 Experiments and experimental results.....	47
6.1 Synthesis of WO _{3-δ} nanorods.....	47
6.2 Scanning electron microscopy investigations.....	51
6.2.1 Mechanism of growth on mica.....	57
6.2.2 Mechanism of growth and orientation on Si(001).....	61
6.3 Chemical homogeneity of the WO _{3-δ} nanorods.....	65
6.4 Chemical stoichiometry and W/O ratio.....	67
6.5 Vibrational properties and sub-stoichiometry.....	70
6.5 Crystallographic properties.....	73
6.6 Optical properties in UV-VIS-NIR properties.....	76
Conclusion	78
References	80



LIST OF FIGURES

1. Typical multilayered WO_3 based electrochromic device for smart windows applications.
2. A US National Renewable Energies Laboratory WO_3 based electrochromic window in its (a) transparent or bleached and (b) opaque or darkened states. *NREL Website, 2006.*
3. Ionic and charge exchanges in a WO_3 based electrochromic smart system.
4. Diffusion constants versus relative density for sputtered tungsten oxide films. Data are given for two levels of proton intercalation (from Wang et al, 1995).
5. Ionic and charge exchange mechanisms in a WO_3 based electrochromic window.
6. Room temperature usual stable monoclinic structure of tungsten trioxide WO_3 (large and small spheres are tungsten and oxygen respectively).
7. Room temperature usual stable structure of tungsten dioxide WO_2 (large and small spheres are tungsten and oxygen respectively).
8. Room temperature stable hydrated tungsten trioxide $\text{WO}_3\cdot\text{H}_2\text{O}$.
9. Shows the color scale compared to the W/O ratio of the crystalline bulk WO_x tabulated from Glemser and Sauer data.
10. Electronic band structure of bulk WO_3 .
11. Calculated band structure for WO_3 in the simplified cubic perovskite-type structure, assuming that the lattice constant $a = 3.85 \text{ \AA}$.
12. The spectrum of electron states calculated by Bullet for the full monoclinic and orthorhombic crystal structures of WO_3 .
13. Ionic and charge exchanges mechanisms in a WO_3 based electrochromic window.
14. Main growth mechanism modes (a) Frank-van der Merwe, (b) Volmer-Weber and (c) Stranski-Krastanow.
15. Thermal evaporator used for the synthesis of the $\text{WO}_{3-\delta}$ nanorods onto Mica, Si(001) and Corning glass ultra-sonicated substrates.

16. Lindberg-horizontal tube type furnace used for the samples' heating in an oxygen rich atmosphere.
17. Scanning electron micrographs of $\text{WO}_{3-\delta}$ nanorods on different substrates at early stage of growth.
18. Influence of surface cleanliness on the texture of the deposited tungsten oxide coatings onto ultrasonically (a) non cleaned and (b) cleaned Corning glass substrates.
19. Scanning electron micrographs of tungsten oxide nanorods deposited during (a) 1 min and (b) 5 min on Mica substrates.
20. Schematic representation of (001) plane of the tetragonal tungsten bronze K_xWO_3 ($0.4 < x < 0.6$), $a = 1.23$ nm, $c = 0.38$ nm.
21. Growth stage of tetragonal tungsten bronze K_xWO_3 ($0.4 < x < 0.6$), $a = 1.23$ nm, $c = 0.38$ nm.
22. Scanning electron micrographs of tungsten oxide nanorods on Si(100) substrate and columnar growth structure.
23. Scanning electron micrographs of $\text{WO}_{3-\delta}$ nanorods on Si(001) substrates for different currents (a) 8A, (b) 10A and (c) 13.5 Amperes.
24. EELS mapping of deposits onto carbon coated grids showing tungsten (W: Blue) and oxygen (O: red).
25. Rutherford Backscattering profile of a dense nanorods deposits onto ultrasonically cleaned Si(001).
26. Room temperature Infrared spectroscopy profiles of (a) bulk WO_3 and (b) dense nanorods deposits on Si(001) substrate.
27. Room temperature XRD profile of the standard WO_3 powder used as a reference and the possible simulated crystalline phases.
28. Texture and spatial orientation of the tungsten oxide nanorods deposited on Si(001) substrates.
29. UV-VIS-NIR optical transmission of $\text{WO}_{3-\delta}$ nanorods coatings on corning glass substrates at different currents: (a) 8A, (b) 10A and (c) 13.5A.

LIST OF TABLES

1. Evolution of the H^+ diffusion coefficient with the sputtered WO_3 for different hydrogen intercalation in H_xWO_3 thin films.
2. Major bulk crystals of WO_3 crystallographic phase structures and their different temperature range of stability: (α - WO_3) tetragonal, (β - WO_3) orthorhombic, (λ - WO_3) monoclinic, (δ - WO_3) triclinic and (ϵ - WO_3) monoclinic.
3. Major stoichiometric and non-stoichiometric bulk crystals of WO_3 crystallographic phases and their lattice parameters.

The outline of this thesis is as follows:

Chapter one gives a general background explaining in details what are WO_3 nanorods. The chapter highlight the aim of the project and why this study is concentrating on nanorods type architecture.

Chapter two provide more insight on the origin of the electrochromism in WO_3 . It further provide a description of the principle of electrochromism in WO_3 . Moreover, the chapter gives the possible mechanism of rearrangement that takes place during WO_3 thin layer diffusion and reaction phases by explaining the possible models.

Chapter will discuss all the properties and phase transitions of bulk WO_3 . Each phase is explained in detail. The optical properties of tungsten oxide is discussed and analyzed in details. Furthermore, the electronic properties of tungsten oxide are discussed.

Chapter four highlight the literature survey and provide the current state of research around the world. Concluding this chapter will be a detailed description on the synthesis mechanism and methodology used to synthesize the WO_3 nanorods.

Chapter five briefly explains the growth mechanisms of WO_3 nano rods

Chapter six will discuss all the experimental set up, the synthesis and characterization will be discussed here. Experimental results are discussed and finally a section that summarizes the findings of chapter six

CHAPTER ONE

1. INTRODUCTION AND AIM OF THE RESEARCH PROJECT

Saving energy in the building sector and automotive industry is a major global socio-economic target in energy efficiency as well as from environmental viewpoint. Substantial savings in energy consumption can be realized through an optimal solar radiations management with the emerging smart photonics in minimizing the usage of air-conditioning systems. With worldwide ≈ 2 billions m^2 of smart photonics coated glass windows, energy saving in the two mentioned air-conditioning segments i.e. buildings and cars, has been estimated to be ~ 1 billion GJ and CO_2 atmospheric emissions would be reduced by ~ 100 millions of tons [1]. The global production of glass which could be solar regulated to minimize the air conditioning using emerging smart nano-photonics, could be a part of 1 billion m^2 /year with about 25% for building and $\sim 11\%$ for automotive industry [1-2]. Examples of these smart photonics include electrochromic tungsten oxide based devices [Figure 1]. These smart windows can be tuned to be transparent or dark in a reversible manner [Figure 2]. Due to such a significant optical modulation, this later nanotechnology with a well established scientific platform could play a key role in energy management in both automotive and architectural sectors as mentioned previously. To set the scene, one has to note that heating, cooling, lighting, ventilation and powering of buildings and automotives account for more than the half of the total energy consumption worldwide and hence responsible for more energy consumption than any other end-user sector such as industrial production. The considered electrochromic smart nano-photonics are also valuable to the Southern African landscapes too. Indeed, the annual global solar radiation average received by South Africa averages $5.5 \text{ kWh/m}^2/\text{day}$, one of the

highest national levels in the world.

Worldwide research is conducted on advanced electrochromic devices for obtaining this optical modulation function through the action of electrical voltage pulses of few volts. As shown in Figure 1, the electrochromic device comprises generally five superimposed thin layers on a transparent substrate (glass or polyester foil) or in between two such materials. The outermost layers deposited on glasses consist of transparent electrical conductors (for example tin doped indium oxide). The three layers in between are made of porous tungsten oxide (WO_3), a transparent ion conductor (electrolyte), and porous nickel oxide (NiO) in general. When an electrical voltage is applied over the outer layers, electrical charge is shuttled between the porous oxide layers whose transparency thereby is changed so that the overall light throughput of the device is altered. The function is similar to that of an electrical “thin film battery” whose charging state manifests itself in optical absorption. Therefore, electrochromic smart windows can be used to achieve a combination of enhanced indoor comfort and energy efficiency in buildings and automobiles. If the device is based on flexible foils, it can be used in visors for motorcycle helmets and in ski goggles. Other applications concern information displays and surfaces with variable heat emission [1-2].

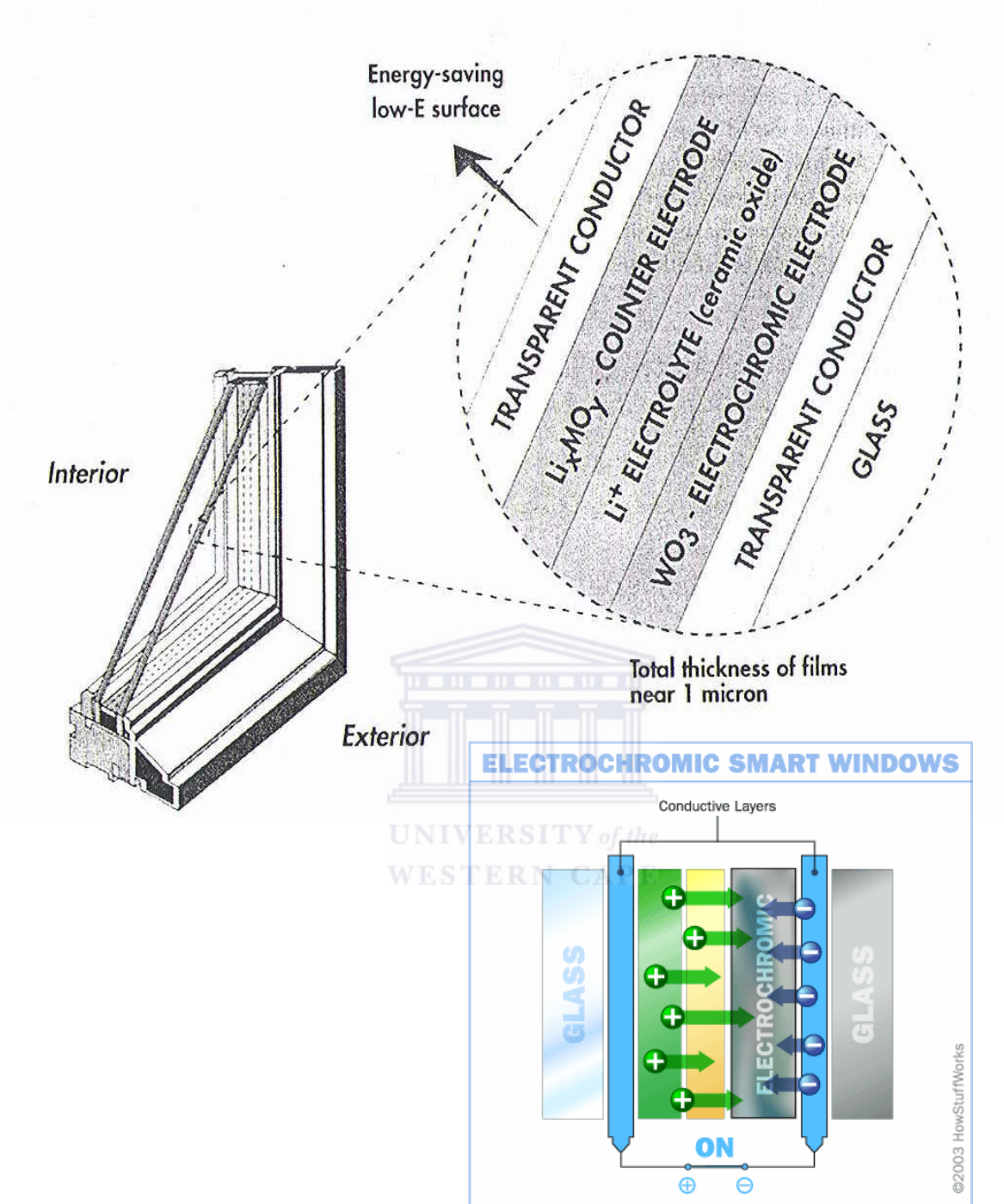


Figure 1
 Typical multilayered WO_3 based electrochromic device for smart windows applications
 [From reference [1]]

**(a)
Transmittive
state**



**(b)
Opaque
state**

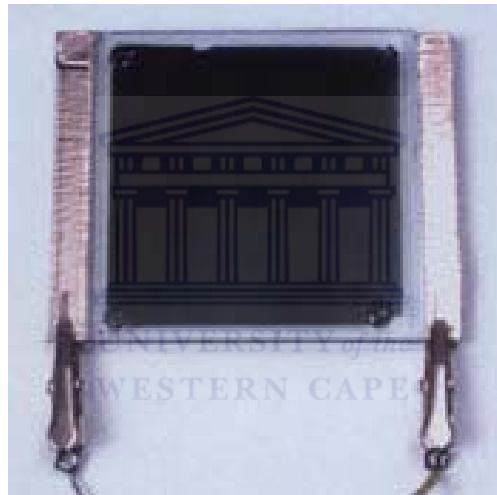


FIGURE 2

A US National Renewable Energies Laboratory WO_3 based electrochromic window in its (a) transparent or bleached and (b) Opaque or darkened states.
NREL Website, 2006

The core component of this smart window is the WO₃ layer. It is widely accepted that the electrochromic process of coloration/bleaching of this WO₃ layer involves simultaneous injection (or extraction) of electrons and charge compensating ions into interstitial sites of the WO₃ matrix as indicated in Figure 3. This leads to the formation of the tungsten bronze M_xWO₃ (where M=H, Li, Na or Cs) with x ≤ 1. Ion intercalation (H⁺, Li⁺, Na⁺ or Cs⁺) into WO₃ gives rise to donor energy levels, which may act as shallow or deep states depending on the values of x and the nature of the intercalated ions. Intercalated WO₃ can have insulating, semiconducting or metallic properties depending on the value of x, thus resulting in large variations of the optical, electrical and structural WO₃ films.

In these electrochromic WO₃ based films, the injection of I-group ions and electrons form tungsten bronze (color centres). The colouration/bleaching rate as well as its switching depend on the size of the intercalated ions as it is related to their ionic diffusion coefficients [Table 1]:

$$\text{H}^+: 10^{-10} < D_{\text{H}^+} < 2.5 \times 10^{-7} \text{ cm}^2/\text{s},$$

$$\text{Li}^+: 1.5 \times 10^{-12} < D_{\text{Li}^+} < 5 \times 10^{-9} \text{ cm}^2/\text{s},$$

$$\text{Na}^+: D_{\text{Na}^+} < 1.8 \times 10^{-16} \text{ cm}^2/\text{s}.$$

Lithium based electrolyte are being the most used due to Lithium ionic radius size (Li⁺ ionic radius ≈ 0.073 nm) [3]. In addition to the intrinsic value of the size of the intercalated ions, the rate of intercalation depends largely on the structure of WO₃ layer. An optimal porous architecture of the WO₃ layer would certainly enhance the rate of intercalation and hence would allow enhanced optical modulation in the Visible-infrared (VIS-IR) and rapid switching; Nano-rods of WO₃ are therefore targeted as a substitute to the continuous film of nanostructured standard of WO₃

architecture. Therefore, this research work focuses on the engineering of nanorods of tungsten oxide as an integrated part of electrochromic devices with high rate optical modulation and fast optical response characteristics.

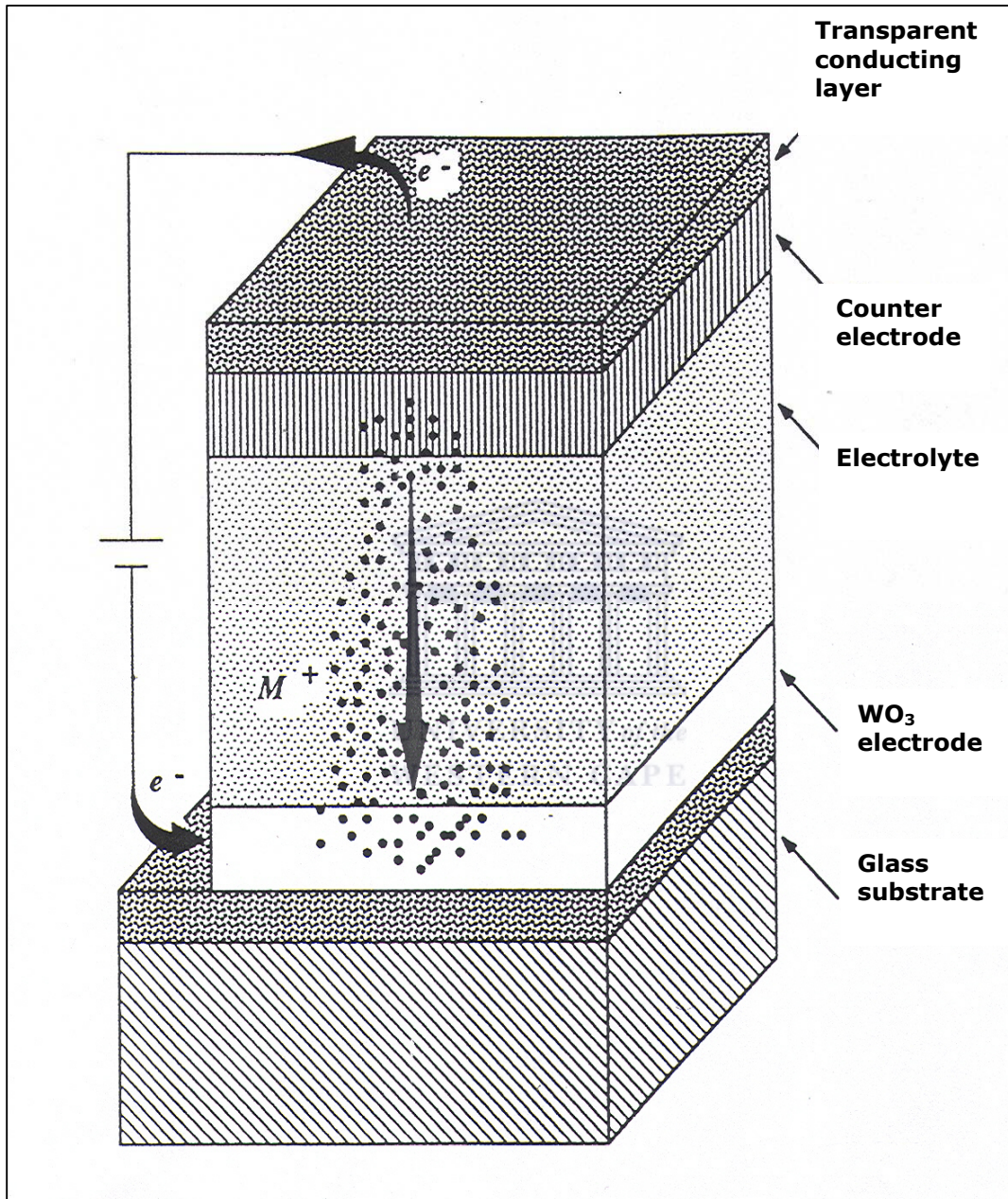


FIGURE 3
Ionic and charge exchanges in a WO₃ based electrochromic smart system.

TABLE 1: Shows the evolution of the H⁺ diffusion coefficient with the sputtered WO₃ for different hydrogen intercalation in H_xWO₃ thin films.

Ionic composition	Relative	Diffusion coefficient
(x)	Density (gm/cc)	(cm²/s)
0.1	0.74	4 x 10 ⁻⁹
0.1	0.82	6 x 10 ⁻¹⁰
0.1	0.89	2 x 10 ⁻¹¹
0.3	0.74	2 x 10 ⁻⁹
0.3	0.82	3 x 10 ⁻¹⁰
0.3	0.89	5 x 10 ⁻¹¹



2. NANOROD ARCHITECTURE SHAPED WO₃

As mentioned previously, the ion intercalation/de-intercalation into WO₃ layers governs the optical modulation and its dynamics in electrochromic tungsten based oxide and therefore their electrochromic efficiency. This efficiency is considered in terms of rate of bleaching/colouration and the speed of this optical modulation. The diffusion coefficient D_{ions} of the ionic species (H^+ , Li^+ , Na^+ or Cs^+) is therefore an important parameter, since it determines the dynamics of the optical change. In addition, the magnitude of D_{ions} depends strongly on the porosity of the WO₃ film in addition of the electrolyte viscosity. Figure 4 reports few data by Wang et al [4] on H^+ diffusion in tungsten oxide films prepared by magnetron sputtering at different plasma pressures so that a range of relative densities were accomplished. Data obtained by impedance spectrometry are reported for two magnitudes of “x” in H_xWO_3 in Figure 4. The effect of increasing porosity is indeed important, and by going from a relative density of ~ 0.9 to ~ 0.75 the value of D_{H^+} is altered significantly from the 10^{-11} - 10^{-10} cm^2/s range up to the 10^{-9} - 10^{-8} cm^2/s range, i.e. by two orders of magnitude. This is a significant difference with regard to possible device performance enhancement and fast optical switching from transparent to opaque state of WO₃ based electrochromic smart windows. The diffusion coefficient drops by about a factor two when “x” is increased from 0.1 to 0.3 if the film is porous, which may be assigned to the blocking channels for ion diffusion. In compact standard tungsten oxide films, the effect of “x” on D_{H^+} seems to be the opposite. Hence the open framework of the architecture of tungsten oxide nanorods/nanowires would allow a high porosity, faster ionic diffusion and likely light trapping effect due to the specific

columnar structure. These effects should permit a faster and larger optical modulation in nanorods/nanowires based tungsten oxide electrochromic devices.

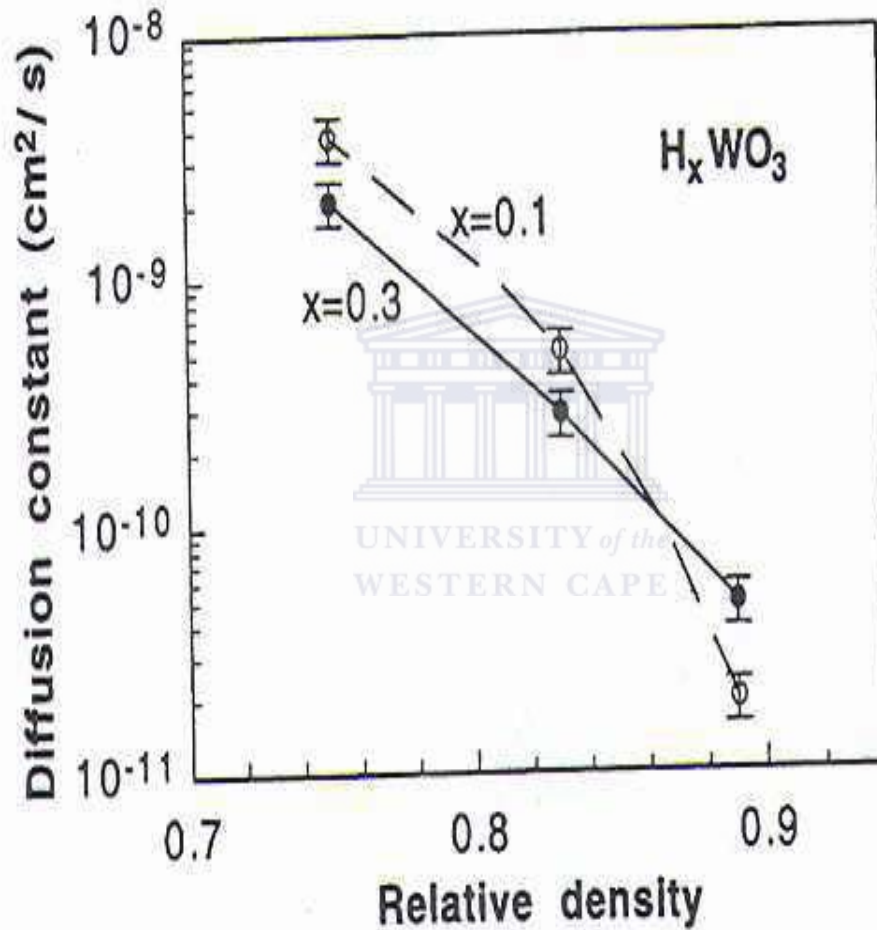


FIGURE 4

Diffusion constants versus relative density for sputtered W oxide films. Data are given for two levels of proton intercalation [4].

CHAPTER TWO

2.1 ELECTROCHROMISM IN WO₃

An ion intercalation electrode is a solid substrate, into which ions can be inserted by the application of a voltage pulse or electric field. Research has been conducted on the properties of tungsten oxide as an ion intercalation electrode since the early 1970's. A publication by Deb in 1969 showed that colour centers could be formed in thin films of tungsten oxide by the application of an electric field [5]. He called the WO₃ film "Electrochromic", a term previously only associated with some organic compounds. The electrochromic properties of transition metal oxides have been extensively studied over the past three decades [6]. Due to many specific properties, tungsten oxide is by far the most promising and widely studied electrochromic material. Thin films of tungsten oxide receive attention due to numerous applications amongst them being the variable transmission smart windows [7], gasochromatics [8], and large flat-panel displays [1].

As mentioned before, the optical transmission in the ultraviolet-visible-near infrared(UV-VIS-NIR) spectral region of tungsten oxides switches from transparent to opaque in response to a small applied voltage of about 2,5 - 3 V. This reversible coloration process is based on the double injection of light ions and electrons to form the tungsten bronze M_xWO₃ (M⁺ = H⁺, Li⁺, etc.) which could be described chemically as:



Figure 1 shows a five-layer typical prototype device which introduces a basic design concepts and types of materials. The middle of the construction contains a purely ionic conductor (electrolyte), either a thin film or a polymeric laminate material; it should be a good conductor for small ions such as H^+ or Li^+ . The electrolyte is in contact with an electrochromic layer and a counter electrode which, for the case of a transparent device, must remain non-absorbing irrespective of its ionic content or exhibit electrochromism in a sense opposite to that of an electrochromic film. Ideally, the electrochromic film (counter electrode) should display cathodic (anodic) electrochromism, or vice versa. This three layer configuration is positioned between transparent electrical conductors. As shown in Figure 3, by applying a voltage over the outer layers, ions can be shuttled into and out of the electrochromic film whose optical properties are changed, thereby modifying the overall optical performance of the device. Physically the optical modulation at least in strongly disordered electrochromic films is due to a variable polaron absorption associated with charge-balancing electrons introduced along with the ions [9].

2.2 ORIGIN OF ELECTROCHROMISM IN WO_3

Although the global mechanism seems to be well established and contributes to the formation of a bronze type tungsten compound, the detailed mechanism and the successive chemical-physical reactions involved are not all understood even within the extensive related literature summarized in numerous review papers by Granqvist [1-3]. Accordingly, there are numerous phases in the process of coloration of the WO_3 thin layer diffusion and reaction phases. As indicated in Figure 5, the first step consists of an injection of electrons and ions so as to ensure the electrical neutrality of

the WO_3 material. During the second phase, a rearrangement takes place at the atomic level between the injected electrons, the inserted ions and the host network ions. As there are injected electrons in the structure of the WO_3 layer, they can be trapped by different sites in the WO_3 bronze network. Hence, a few possible mechanisms of rearrangement were proposed:

Model 1:

The injected electron resides localized on the inserted ion M^+ to form an interstitial atom M in the host structure.

Model 2:

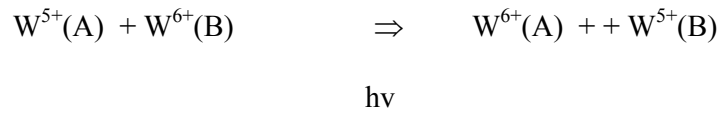
The injected electron can be trapped in lacunar oxygen to form a coloured centre as proposed by Deb in the earlier period of electrochromism in WO_3 [9]. Effectively, the oxide which is sub-stoichiometric $\text{WO}_{3-\delta}$, presents a certain degree of positively charged ionic defects. The then trapped electron would occupy the d orbital of tungsten atoms close to lacunar oxygen, therefore reducing each W^{6+} to W^{5+} and M^+ stays ionized in an interstitial site.

Model 3:

The injected electron remains delocalized in the conduction band of WO_3 while M^+ is still ionized in an interstitial site. It is the hypothesis proposed by Green et al [10] in which the electrons are considered as a gas of free electrons.

Model 4:

The injected electron is localized on a tungsten site to form an ion W^{5+} , the M^+ remains ionized in a preferential site as suggested by Faughnan et al [11]. The observed optical absorption is explained by an electronic transfer between two sites of neighboring W, (A) and (B) following the scheme:



Model 5:

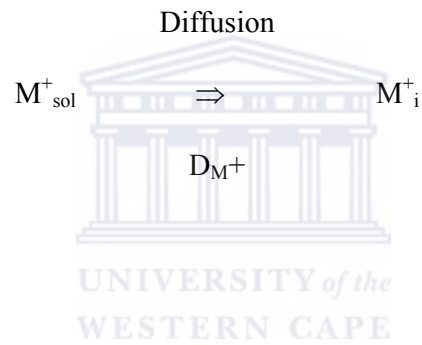
An injected electron can be localized on a particular site of the network. The interaction between this electronic charge and the surrounding environment would form a polaron. The observed optical absorption is therefore from a polaronic nature within the amorphous host matrix.

Model 6:

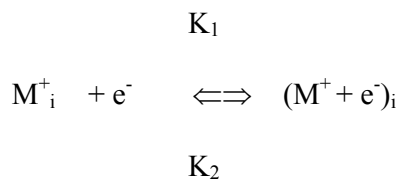
From the previous models consisting of a double injection (ionic and electronic) and the formation of W^{5+} responsible for the colouration of the tungsten oxide layer as well as the existence of numerous reaction successive phases, Bohnke et al [12] have suggested an additional comprehensive model. This model allows one to calculate the optical density and current density within the WO_3 layer. In addition, it permits the determination of the limiting phases of these two parameters. Figure 5 illustrates this model and indicates the different steps involved. The first consists of the diffusion of

M^+ ions in the electrolyte. The second is an electrochemical reaction at the interface WO_3 electrolyte which gives an ion and an electron close spaced, called hereafter an ion-electron entity. The third phase is the diffusion of this entity within the WO_3 layer. The fourth phase is a rearrangement of the diffusing entity to give birth to an ion M^+ , immobilized in an interstitial site of the host matrix, a trapped electron either on a W site or lacunar oxygen and an ion W^{5+} . The fifth reaction represents possible undesirable reactions such as metallic deposition of M or hydrogen emission if M^+ is H^+ . In this model, the previous steps could be summarized as:

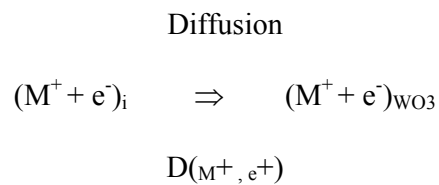
Phase 1



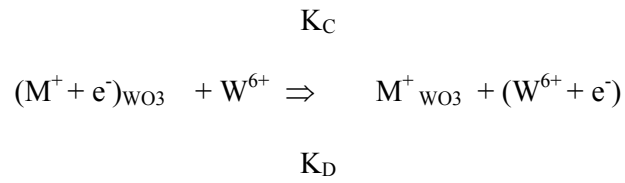
Phase 2



Phase 3



Phase 4



M^+_{sol} : M^+ in the electrolyte

M^+_i : M^+ at the interface WO_3 -electrolyte

$(M^+ + e^-)_i$: Reduced M^+ or ion-e at the interface WO_3 -electrolyte

$(M^+ + e^-)_{WO_3}$: Reduced M^+ or ion-e in WO_3 host layer

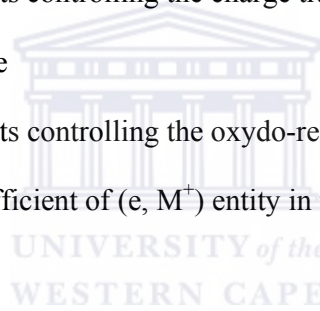
$M^+_{WO_3}$: immobilized M^+ in WO_3 host layer

D_{M^+} : Diffusion coefficient of M^+ in the electrolyte

K_1, K_1 : Speed constants controlling the charge transfer at the interface
 WO_3 -electrolyte

K_C, K_D : Speed constants controlling the oxydo-reduction reaction

$D_{(M^+, e^+)}$: Diffusion coefficient of (e, M^+) entity in the WO_3 layer



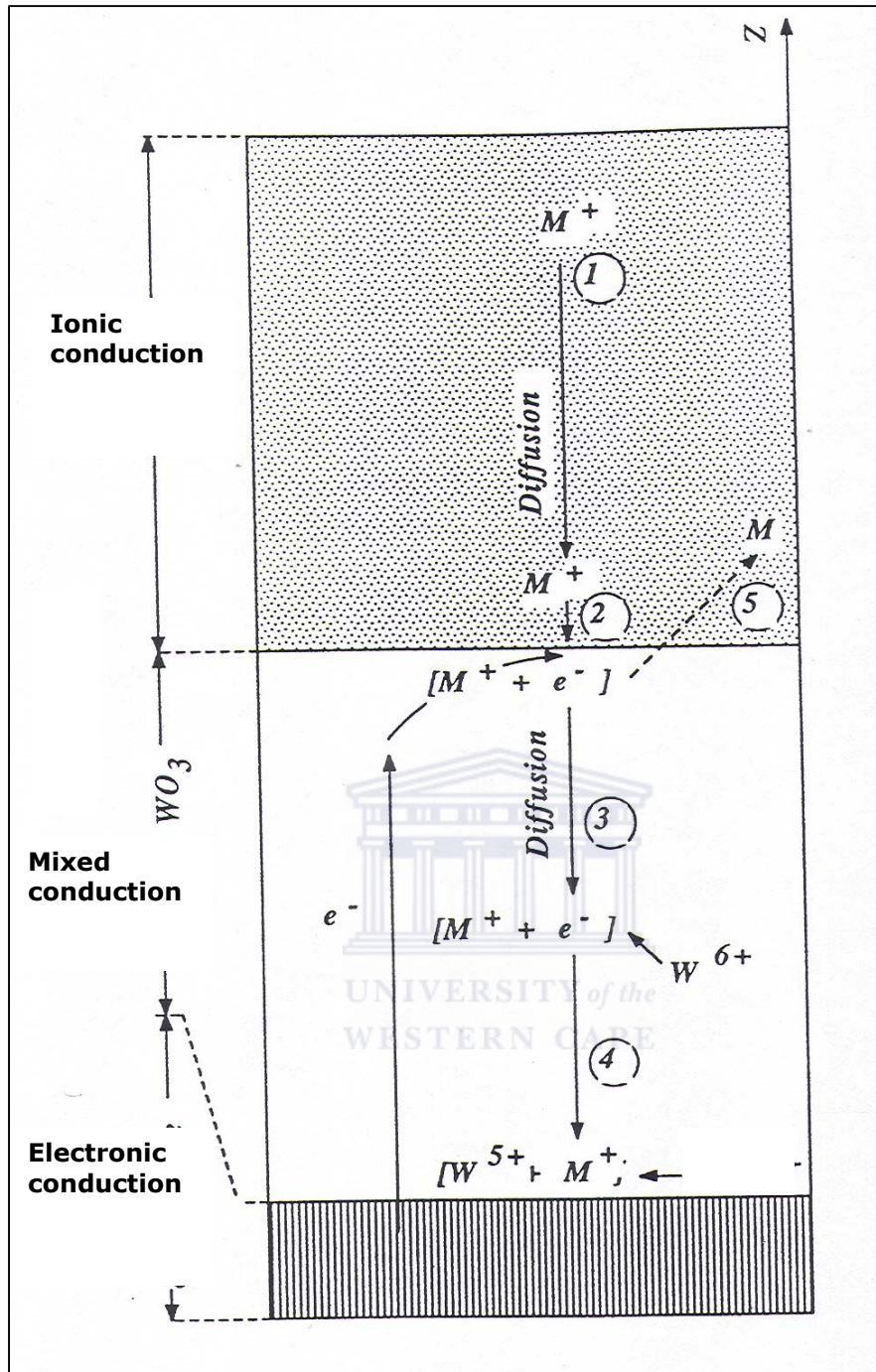


FIGURE 5: Ionic and charge exchanges mechanisms in a WO_3 based electrochromic window.

CHAPTER THREE

3.1 STRUCTURAL PROPERTIES AND PHASE TRANSITIONS OF BULK WO_3

Bulk tungsten trioxide WO_3 exhibits perovskite-type structures based on the corner-sharing of WO_6 octahedra as shown in Figure 6. On the other hand, structural analysis of WO_3 have revealed considerable deviations from the ideal cubic perovskite type, the distortions corresponding to antiferroelectric displacements of W atoms and mutual rotations of the oxygen octahedral. As in most perovskite-like compounds, the magnitude of the distortion depends on the temperature. Difficulties in obtaining good single crystals, and hence good structural data, are compounded by the tendency of WO_3 to form sub-stoichiometric shear phases in the range WO_3 to $\text{WO}_{2.87}$ [13] containing edge-sharing octahedra. In these phases crystallographic shear planes, which occur also in other transition metal oxides such as MoO_3 and TiO_2 , provide a mechanism for altering the anion to cation ratio without changing the coordination polyhedron of oxygen and without introducing point defects [14]. More accurately, the sub-stoichiometric phases in bulk crystalline tungsten oxides have a tendency to form organized phases in the series of $\text{W}_m\text{O}_{3m-1}$ and $\text{W}_m\text{O}_{2m-2}$ ($m=1, 2, 3, 4\dots$) but also slightly different phases like $\text{W}_{18}\text{O}_{49}$ and $\text{W}_{40}\text{O}_{116}$. With WO_2 which has the structure depicted by Figure 7, stoichiometric tungsten oxide WO_3 is made from WO_6 building blocks with octahedrally tungsten ions located and surrounded by six oxygen ions with each oxygen right between two tungsten ions [Figure 6]. In this stable trioxide, which is transparent in a thin film form, each oxygen ion is shared by two corner

shaded blocks, while in the WO_2 form which is brown in a thin film, each oxygen ion is shared by three edge-shared blocks [Figure 7]. In fact single crystals of WO_3 do exhibit a very rich crystallographic phase structures in different temperature ranges: (α - WO_3) tetragonal, (β - WO_3) orthorhombic, (λ - WO_3) monoclinic, (δ - WO_3) triclinic and (ε - WO_3) monoclinic. Their domain of stability is reported in the following

Table 2:

TABLE 2: Shows Major bulk crystals of WO_3 crystallographic phase structures and their different temperature range of stability: (α - WO_3) tetragonal, (β - WO_3) orthorhombic, (λ - WO_3) monoclinic, (δ - WO_3) triclinic and (ε - WO_3) monoclinic. [16,47]

Phase	Crystallographic structure	Stable temperature range ($^{\circ}\text{C}$)
α - WO_3	Tetragonal	>740 722 720 ~680
β - WO_3	Orthorhombic	480 320
λ - WO_3	Monoclinic	> 200
δ - WO_3	Triclinic	-40
ε - WO_3	Monoclinic	

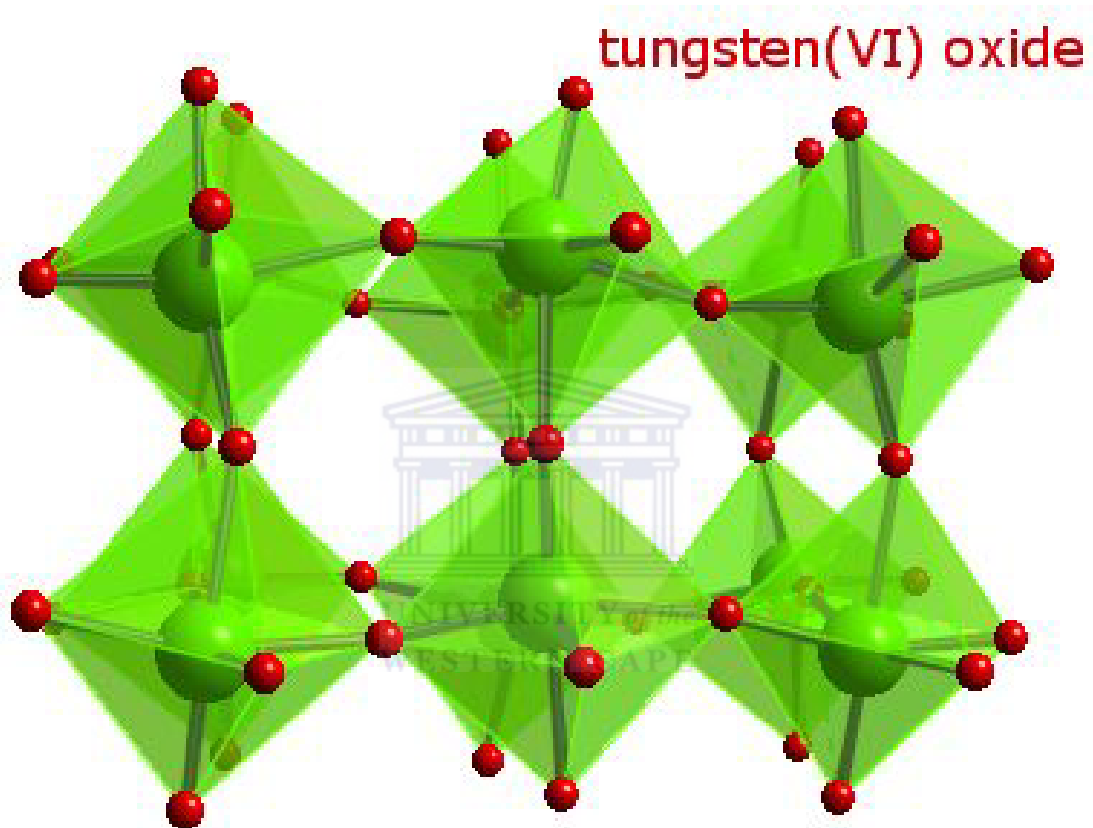


FIGURE 6: Room temperature usual stable monoclinic structure of tungsten trioxide WO_3 (large and small spheres are tungsten and oxygen respectively) [From 40].

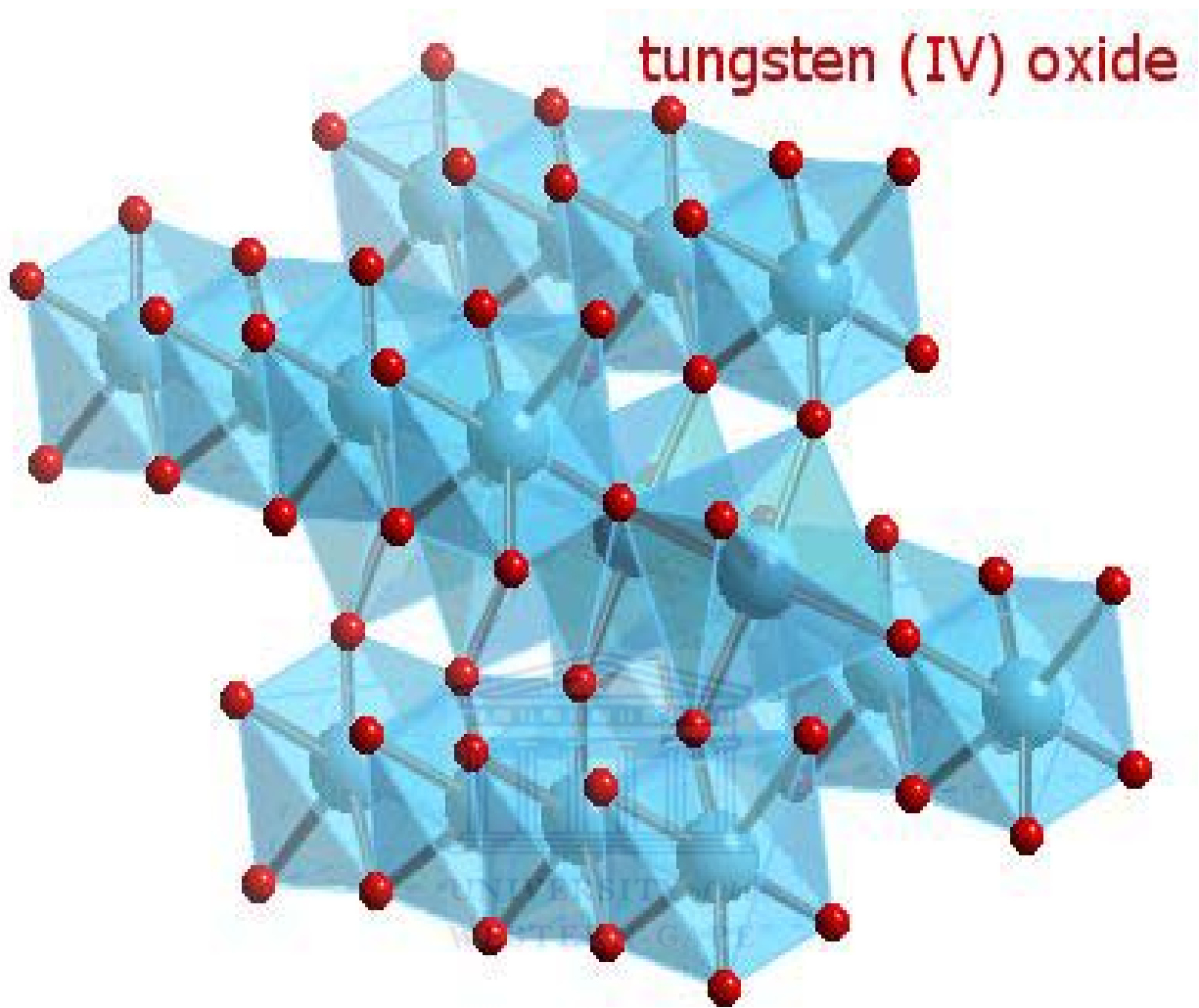


FIGURE 7
Room temperature usual stable structure of tungsten dioxide WO_2 (large and small spheres are tungsten and oxygen respectively) [From 40].

TABLE 3: gives the major structures of both stoichiometric and non stoichiometric tungsten trioxides in their bulk showing the intensity of their stable phases (from International JCPDC database)

JCPDC file number	Oxide	Crystallographic structure	Strong peaks at $\lambda = 1.54059\text{\AA}$ 2θ (deg)	Miller indexation (h k l)
2-310	WO ₃	Triclinic a = 7.280 b = 7.480 c = 3.820 $\alpha = \beta = \gamma = 90^\circ$	23.144 33.280 34.605	(001) (0-21) (-2-21)
5-431	WO ₂	Monoclinic a = 5.650 b = 4.890 c = 5.550 $\alpha = \gamma = 90^\circ$, $\beta = 120.40^\circ$	25.803	(-110)
5-392	W ₁₈ O ₄₉	Monoclinic a = 18.280 b = 3.775 c = 13.980 $\alpha = \gamma = 90^\circ$ $\beta = 115.20^\circ$	23.517	(010)
5-386	W ₂₀ O ₅₈	Monoclinic a = 12.050 b = 3.767 c = 23.590 $\alpha = \gamma = 90^\circ$, $\beta = 94.72^\circ$	23.580	(010)
5-363	WO ₃	Monoclinic a = 7.285 b = 7.517 c = 3.835 $\alpha = \gamma = 90^\circ$, $\beta = 90.15^\circ$	23.175 24.421	(001) (200)
2-414	WO ₂	Tetragonal a = 4.860 b = 4.860 c = 2.770	25.879	(110)
84-1516	W ₁₈ O ₄₉	Monoclinic a = 18.318	23.499	(010)

		b = 3.782 c = 14.028 $\alpha = \gamma = 90^\circ$, $\beta = 115.21^\circ$		
83-950	WO ₃	Monoclinic a = 7.301 b = 7.538 c = 7.689 $\alpha = \gamma = 90^\circ$, $\beta = 90.89^\circ$	24.367	(200)
83-949	WO ₃	Triclinic a = 7.310 b = 7.524 c = 7.685 $\alpha = 88.85^\circ$ $\gamma = 90.93^\circ$, $\beta = 90.91^\circ$	23.638	(020)
83-948	WO ₃	Triclinic a = 7.312 b = 7.525 c = 7.689 $\alpha = 88.85^\circ$ $\gamma = 90.94^\circ$, $\beta = 90.91^\circ$	24.330	(200)
81-2263	W ₃ O ₈	Orthorhombic a = 10.350 b = 13.990 c = 3.780	23.517	(001)
81-2262	W ₃ O ₈	Base-centered orthorhombic a = 6.386 b = 10.430 c = 3.800	23.391	(001)
81-558	WO _{1.09}	Base-centered orthorhombic a = 17.160 b = 5.160 c = 3.780	42.382	(021)
79-171	W ₁₇ O ₄₇	Monoclinic a = 18.840 b = 3.787 c = 12.330	23.472	(010)

		$\alpha = \gamma = 90^\circ$, $\beta = 102.67^\circ$		
73-2182	WO _{2.90}	Monoclinic a = 12.100 b = 3.780 c = 23.400 $\alpha = \gamma = 90^\circ$, $\beta = 95.0^\circ$	23.517	(010)
73-2177	WO _{2.72}	Monoclinic a = 18.320 b = 3.790 c = 14.040 $\alpha = \gamma = 90^\circ$, $\beta = 115.20^\circ$	23.454	(010)
72-1465	WO ₃	Monoclinic a = 7.300 b = 7.530 c = 7.680 $\alpha = \gamma = 90^\circ$, $\beta = 90.90^\circ$	23.147	(002)
71-2450	W ₁₈ O ₄₉	Monoclinic a = 18.334 b = 3.786 c = 14.44 $\alpha = \gamma = 90^\circ$, $\beta = 115.20^\circ$	23.479	(010)
71-131	WO ₃	Orthorhombic a = 7.341 b = 7.570 c = 7.754	24.229	(200)
71-70	W ₂₅ O ₇₃	Monoclinic a = 11.930 b = 3.820 c = 59.720 $\alpha = \gamma = 90^\circ$, $\beta = 98.30^\circ$	23.267	(010) (011)

3.1.1 Monoclinic structure of WO₃

Monoclinic tungsten trioxide is regarded as the room temperature stable form of WO₃. The temperature transition of monoclinic and triclinic WO₃ is frequently given as 17°C, and this is not a thermodynamic equilibrium transition temperature. The equilibrium transition temperature is higher than 25°C. When cooling WO₃ from high temperature, a pure monoclinic WO₃ is obtained at 25°C [15]. If monoclinic WO₃ is cooled well below room temperature, for example to 5°, it quickly converts to triclinic WO₃. At the same time, on warming triclinic WO₃ to about 25°C, it is stable for an indefinite period at room temperature. The changes in different symmetries of WO₃ or modifications occur with the increase or decrease in temperature. Monoclinic structure has the space group P2₁/n as shown in table 3, with unit cell parameters $a = 7.301$, $b = 7.539$, $c = 7.690 \text{ \AA}$, and $\beta = 90.89^\circ$, and the triclinic structure has the space group P1, with similar cell dimensions, $a = 7.313$, $b = 7.525$, $c = 7.689 \text{ \AA}$, $\alpha = 88.85$, $\beta = 90.91^\circ$, and $\gamma = 90.94^\circ$. Both these structures have been found to undergo a first-order transition [16]. Triclinic structure is considered by Xu [16] to be the most stable thermodynamically form at ambient temperature. Most of the other low- and high-temperature WO₃ modifications have structures closely related to this triclinic form. A transition from the monoclinic to the triclinic as the temperature is increased, involves both small changes of the tungsten positions and a small change of the packing pattern to give a monoclinic unit cell having $\alpha = \gamma = 90^\circ$. In the paper written by Cazzanelli et al [17], it is suggested that there is a small difference in the lattice parameters between the two phases. It is further stated that, by using the XRD results, the changes in diffraction peaks mainly at about $2\theta = 34^\circ$ allows for a clear attribution of the samples to different crystal structures. Literature[18] agrees that

Raman Spectroscopy gives clear evidence of the phase changes and allows to follow the different steps of the transformation by analyzing the evolution of the lowest peaks (up to 100 cm^{-1}) of the Raman Spectra. These peaks correspond to lattices modes of vibrational nature and are noticeably affected by the transition between the low symmetry phases of WO_3 , which involve mainly collective rotations of the basic WO_6 octahedral units [19]. The Raman Spectra show different features in the Υ - and δ -phases [17]. The 34 cm^{-1} peak is typical of monoclinic Υ -phase, while the 43 cm^{-1} peak characterizes the triclinic δ -phase.

3.1.2 Orthorhombic Structure of WO_3

The transition from triclinic to orthorhombic crystal structure of WO_3 is thermally driven. In the analysis made by Cazzanelli using Raman spectroscopy on orthorhombic crystals, numerous vibrational modes were identified:

$12A_g + 6B_{1g} + 12B_{2g} + 6B_{3g}$. The orthorhombic structure has been found to occur between 600K and 1170K [20], with the lattice parameters $a = 7.384$, $b = 7.512$ and $c = 2.770\text{ \AA}$ with a space group Pmnb . The phase transformation from orthorhombic to tetragonal undergoes a phase transition specifically as a function of the oxygen content. The transformation from the oxygen rich orthorhombic phase to oxygen-deficient tetragonal phase occurs as the temperature increases. A number of experiments have demonstrated that nanostructured WO_3 are interesting for their sensing properties and those non-stoichiometric structures are involved in the mechanism of film conductivity because of the free electrons originating from oxygen vacancies.

3.1.3 Tetragonal structure of WO₃

Tetragonal phase of tungsten oxide occurs at high temperatures above 740 °C to the melting point [21]. The crystal structure has the space group P4/nmm with the unit cell parameters $a = 4.860 \text{ \AA}$ and $c = 2.770 \text{ \AA}$. The sequence of temperature-induced phase transitions in WO₃ has been rationalized in terms of changes in the octahedral tilt system and displacements of the tungsten out of the center of the WO₃ octahedron. Above room temperature the phase transition is driven by successive softening of phonon modes, M₃ at the α -WO₃ to β -WO₃ transition and R₂₅ at the β -WO₃ to γ -WO₃ transition [22]. Most work was done on the tetragonal α -WO₃, the results of such conducted experiments has been obtained using different analyzing techniques. The phases identified by Tom [22] between room temperature and 850°C, were found and characterized by Rietveld refinements. Tom and his team obtained two phases in the temperature range: orthorhombic β -WO₃ with the space group Pbcm, lattice parameters $a = 7.3331$, $b = 7.5733$, $c = 7.74013 \text{ \AA}$ at the temperature of about 350°C. The second phase was found to be tetragonal α -WO₃ with the space group P4/ncc, $a = 5.2759$, $b = 5.2759$, $c = 7.8462 \text{ \AA}$ at the temperature of about 850°C.

3.1.4 Hexagonal phase structure of WO_3

The hexagonal form of tungsten trioxide, h- WO_3 synthesized by Gerand et al [23] by dehydration due to dry heating of the hydrate $\text{WO}_3 \cdot \frac{1}{3}\text{H}_2\text{O}$ is depicted in Figure 8. This form of tungsten oxide has been extensively investigated especially for intercalation host for obtaining hexagonal tungsten bronzes M_xWO_3 and a material for the positive electrode of rechargeable lithium batteries. The corner sharing (W-O_6) octahedra form hexagonal channels oriented along the c axis. According to the results of Gerand [23], the structure of h- WO_3 is described to have the space group $\text{P6}/\text{mmm}$ with cell parameters $a = 0.7298 \text{ nm}$ and $c = 0.7798 \text{ nm}$. These results were analyzed using the x-ray diffraction technique.



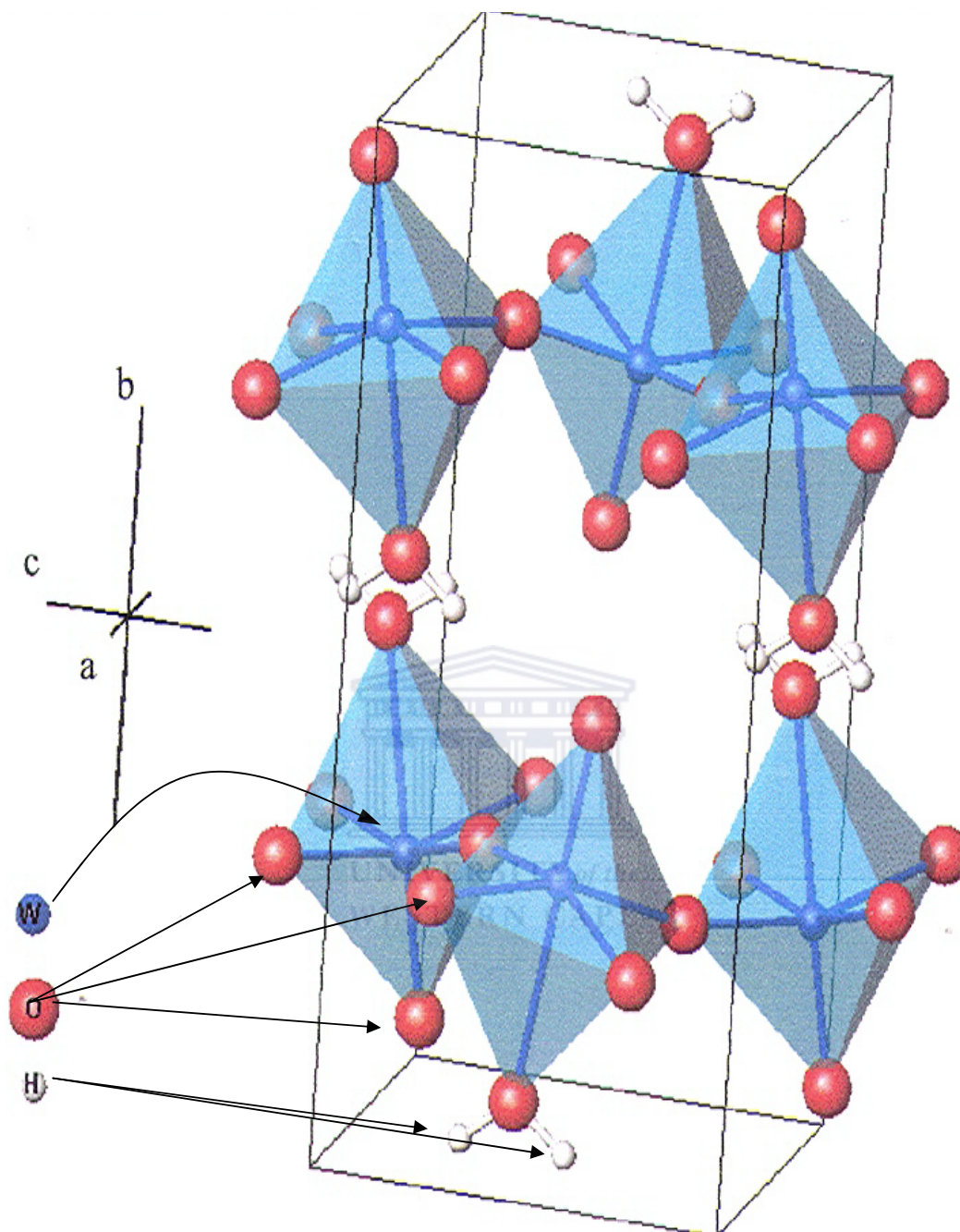


FIGURE 8
Room temperature stable hydrated tungsten trioxide WO₃·H₂O. (From www.ill.fr)

3.2 OPTICAL PROPERTIES

3.2.1 UV-Visible spectral range

From a UV-VIS optical viewpoint, tungsten oxide is a semiconductor compound with an optical band gap of about 3.55 eV for the crystalline phase with a refractive index ranging from 2.25 -2.55 [1]. Similarly, the optical band gap was found to be about 3.1 eV for amorphous tungsten oxide and a refractive index value varying from 2.3 – 2.4 for good electrochromic films. This follows earlier findings that amorphous samples have lower density than the crystalline ones, of about 6.1 g/cm³ and 6.7 g/cm³ respectively. However, the band gap for similar deposited films tends to decrease from 3.17 eV to 3.08 eV as the sputter gas flow increase; consequently the refractive index was found to be approximately 2.2. The relation of the decreased band gap when the oxygen gas flow increase was confirmed and it was found that the band gap can decrease from 3.1 eV to 2.98 eV and the refractive index were about the same. As one could expect, the optical properties of tungsten oxide would be highly affected by the stoichiometry in connection with the state of electronic valence variations in the UV-VIS spectral range.

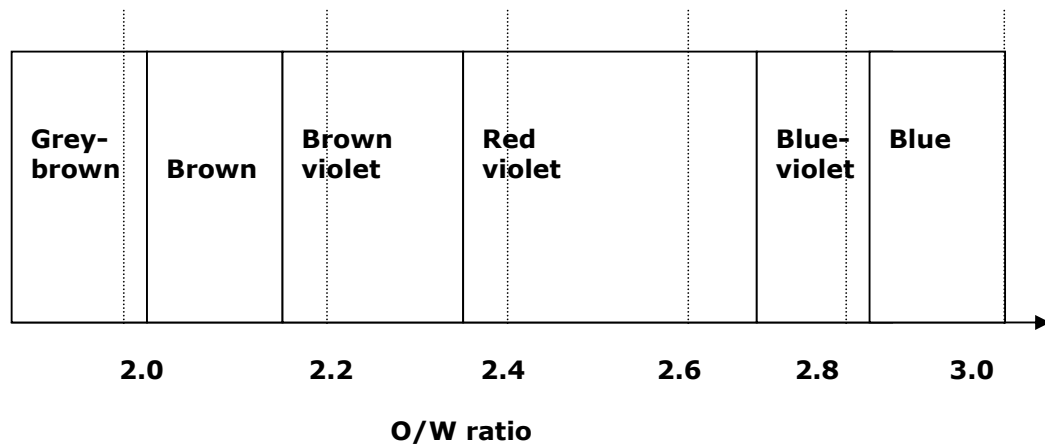


FIGURE 9

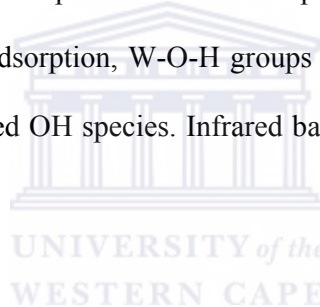
Shows the color scale compared to the W/O ratio of the crystalline bulk WO_x tabulated from Glemser and Sauer data [24].

From figure 9, the color of crystalline tungsten oxide ranges from blue to grayish when the W/O ratio decreases from ~ 3.0 . The color changes in thin films at different compositions are much weaker than in bulk form due to much smaller film thickness, and hence smaller optical absorption. Thin films of tungsten oxide by the sputtering technique have been found to be transparent and metallic when O/W ratio is >2.6 and <2.5 respectively while coloured blue in between [25].

3.2.2 IR spectral range

From an infrared viewpoint, tungsten oxide thin films exhibit two well defined longitudinal optical modes in addition to two transversal modes which are located at 50meV/123 meV and 85 meV/102 meV respectively [26-27]. From Raman spectroscopy studies, it can be found that there are absorption bands at 717 cm^{-1}

(90 meV) and 806 cm^{-1} (100 meV) that are assigned to W-O stretching vibrations and bands at 271 cm^{-1} (33meV) and 327 cm^{-1} (40meV) that have been assigned to W-O bending vibrations [3]. The vibration frequencies at 720 and 330 cm^{-1} were found to be temperature dependent due to phase transformations. Comparisons of tungsten oxide crystal vibration spectra with amorphous spectra showed that the peaks were much broader in the amorphous state and that an additional peak, ascribed to asymmetric stretching vibration modes of double bonds W=O, appeared at 960 cm^{-1} (120meV). Due to the open crystallographic structure of tungsten oxides, the sensitivity to H_2O and OH radicals in particular is effective as shown by both Raman and infrared spectroscopy studies. Ageing studies of water absorption due to exposure to water vapor in air have been performed on amorphous W oxide films. It was concluded that during water adsorption, W-O-H groups are produced with stretching and bending of strongly bonded OH species. Infrared bands were found around 3200 cm^{-1} (397 meV).



3.3 The electronic structure and properties of bulk WO_3

An energy level diagram of the two tungsten oxides can be drafted as shown in Figure 10. It illustrates an oxygen valence band of 2s and 2p orbitals and the 5d, 6s and 6p tungsten conduction band. For WO_3 , the 24 electronic states per WO_3 unit are filled in the oxygen valence band. The Fermi level is in the band gap since the oxide has the same number of valence electrons. It is optically transparent in this state. The Fermi level shifts towards the 5d orbitals of tungsten when external ions and electrons diffuse into the oxide. This induces a blue coloration of the oxide. The level moves downwards when the ions and electrons are removed and the state is transparent

again. For WO_2 the total 16 electrons states per unit are filled in the oxygen valence band with the Fermi level being in the 5d conduction band of tungsten since the oxide has two more electrons per formula unit. It is dark in this state. As a consequence, WO_3 is anodic.

In the bulk, pure tungsten oxide has an indirect band gap of 2.7eV. The properties of this metal oxide depend more closely on its bulk and surface properties, and as a result some of its applications are not intrinsic to WO_3 . For sufficiently high concentrations of the interstitial ions, these bronzes become metals and in some other cases, they become superconductors [28]. WO_3 is a compound with a strong ionic character. In a simplified picture, all six W valence electrons are transferred to the O atoms, which can accommodate two additional electrons each, leading to the formation of an insulator at the stoichiometric WO_3 [29]. Figure 11 shows the calculated band structure for WO_3 in the simplified cubic perovskite-type structure, assuming that the lattice constant $a = 3.85 \text{ \AA}$. These results were conducted by Bullet [30] who compared their finding with the early study by [31]. The calculated semiconducting energy gap of 1.5 eV is smaller than that in the true material.

The orbital decomposition of total density of states for cubic WO_3 has been investigated into various components: the oxygen and tungsten contributions and the separate t_{2g} and e_g orbital components of the tungsten density of states. The e_g ($d_{x^2-y^2}$ and d_{z^2}) W orbitals are those which point directly towards the surrounding O atoms in the perovskite-like structure, while the t_{2g} set (d_{xy} , d_{yz} , d_{zx}) point between the coordinating ligands. The oxygen orbitals are seen to predominate in the s-like band, centered at $\sim -26.5 \text{ eV}$, and the p-like valence band extending from -10.2 to -16.2 eV [30]. Tungsten e_g orbital contribute significantly to the bonding state at the bottom

valence bands, and most of their corresponding weight is forced far up in energy into the broad W-O anti-bonding bands above -5.2eV. The remaining W t_{2g} orbitals have only π -type interactions with the neighbouring anions and it cannot participate in the O s-band and interact only with the weakly O p-orbitals. Bullet further considered the monoclinic and orthorhombic structures, whereby the calculated spectrum of electron states in these structures shows a significant modifications when considering the crystallographic arrangements of WO_3 [Figure 12]. The non cubic distortion cause an increase in the W d-orbital occupation and the calculated gap increases at the zone centre to 1.7 eV for an orthorhombic structure or 2.4 eV for a monoclinic structure.



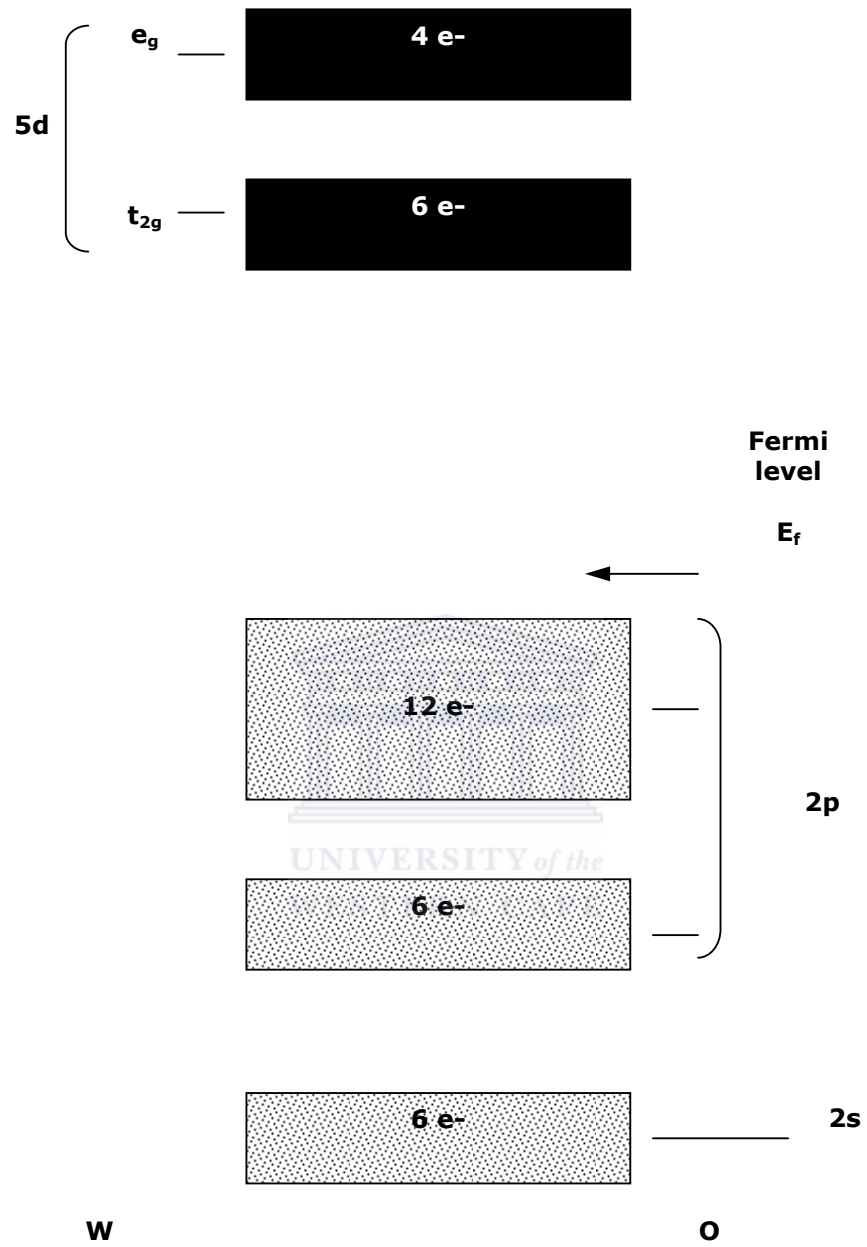


FIGURE 10
Electronic band structure of bulk WO_3 .

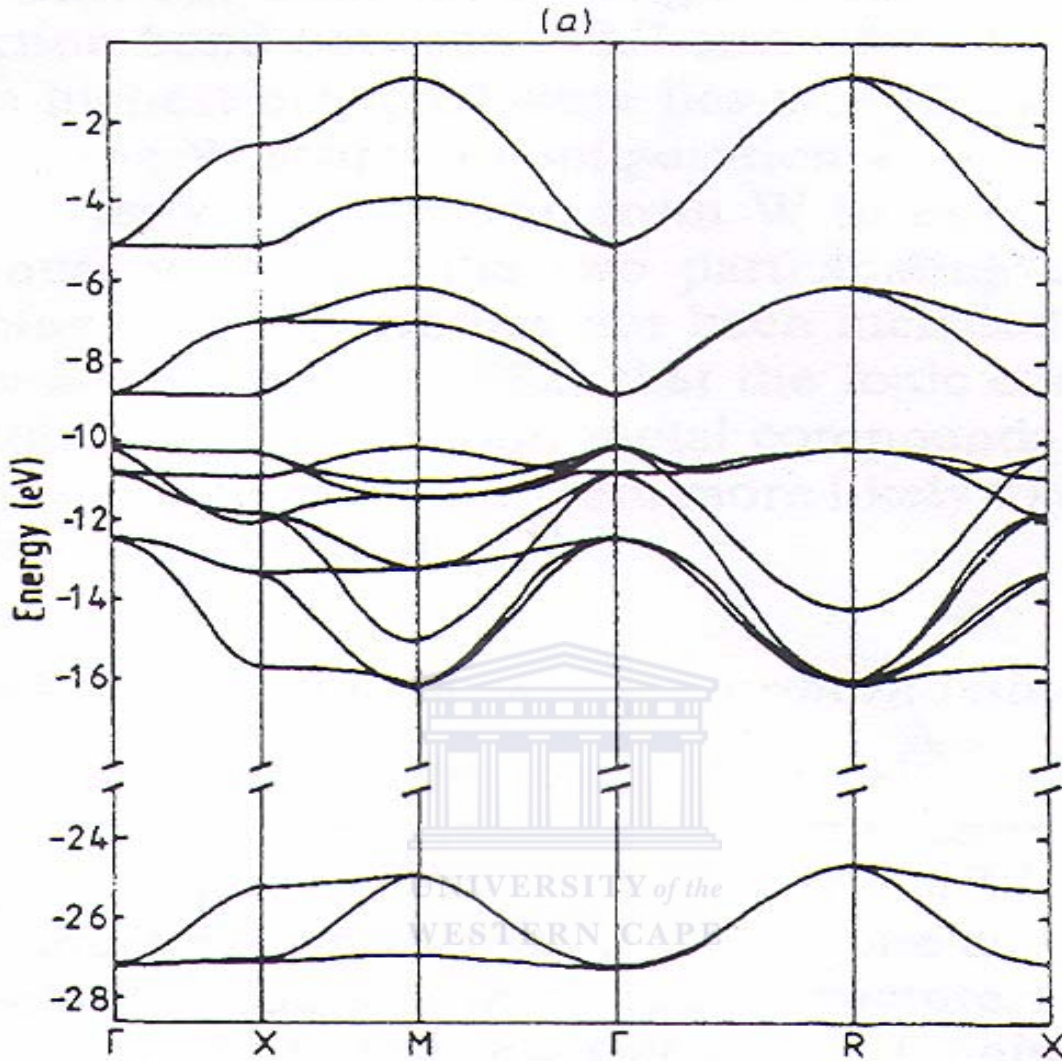


FIGURE 11

Calculated band structure for WO_3 in the simplified cubic perovskite-type structure, assuming that the lattice constant $a = 3.85 \text{ \AA}$ [30].

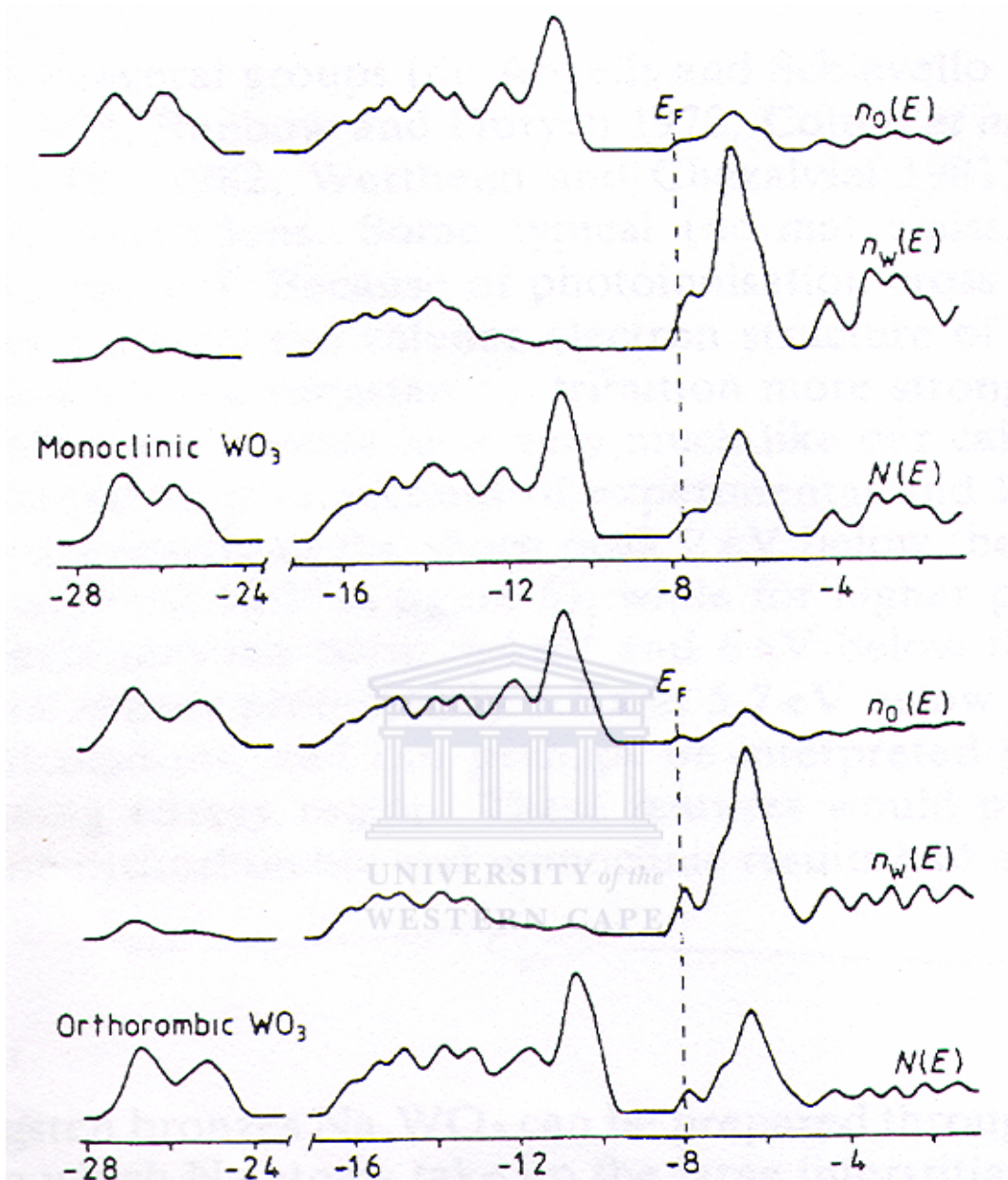


FIGURE 12

The spectrum of electron states calculated by Bullet for the full monoclinic and orthorhombic crystal structures of WO_3 [30].

CHAPTER FOUR

4.1 LITERATURE SURVEY OF WO_{3-δ} NANORODS SYNTHESIS

In correlation to their ionic transport properties and high degree of sensing properties, stoichiometric or non-stoichiometric WO₃ nanorods have been synthesized by diverse methodologies among them one could cite the following recent published research.

4.1.1 Atomic force microscope approach

Gu et al [32] have reported recently that by heating a tungsten tip in Ar atmosphere at around 700°C, isolated tungsten oxide nanowires can be grown directly on the tungsten tip. This provides a simple approach to prepare nanosized WO_x. However, the tungsten oxide nanowires produced were grown at relatively high temperature ~700°C, and were grown and aligned on planar substrates like Si or glass, which is a requirement for their technological applications.

4.1.2 Thermal evaporation

Recently, Liu et al [33] have succeeded to achieve a low-temperature synthesis of large-scale arrays of aligned tungsten oxide nanorods on planar substrates. They have used a simple oxidation approach. By passing a current of about 50A through a tungsten spiral coil in a vacuum of 4×10^{-2} mbar, single-crystalline WO_{2.9} nanorods, ~20nm in diameter and ~ 400 nm long, were deposited on planar substrates on silicon Si(001), Si(111), SiO₂/Si, glass, and Ag-coated silicon substrates at temperatures below 200°C. The nanorods were vertically aligned on the substrates. This methodology, which has been considered within the framework of this research project, provides an easy way to grow large-scale arrays of aligned WO_{3-δ} nanorods at

relatively low temperatures, which might also be applicable to the growth of other metal oxides.

4.1.3 Template methodology

Deepa et al [34] have used a template methodology to synthesize elongated and percolated WO₃ rod-like system. In this case, a potential driven self-assembly of sodium dodecyl sulfate/tungsten oxide aggregates at the electrolyte–electrode interface followed by template extraction and annealing yielded mesoporous thin films of electrochromic tungsten oxide (WO₃). Electron microscopy images revealed that the films are characterized by a hitherto unreported hybrid structure comprising nanoparticles and nanorods with a tetragonal crystalline phase of WO₃ with the measured lattice parameters: $a = 0.53$ nm and $c = 0.37$ nm. In addition to pentagonal voids characteristic of the tetragonal WO₃ phase at the lattice scale, open channels and pores of 5–10 nm in diameter lie between the nanoparticles, which cumulatively promote rapid charge transport through the film. This resulted in colouration efficiency ($\eta_{\text{max}} \sim 90$ cm² C⁻¹ at $\lambda = 900$ nm) and switching kinetics (colouration time = 3 s and bleaching time = 2 s for a 50% change in transmittance) higher and faster than previously reported values for mesoporous WO₃ films. Repetitive cycling between the clear and blue states has no deleterious effect on the electrochromic performance of the film, which is suggestive of its potential as a cathode in practical electrochromic windows.

4.1.4 Sputtering

By sputtering in a reactive atmosphere, Chen et al [35] have succeeded to synthesize oxygen deficient tungsten oxide nanowires. More precisely, the self-synthesis of tungsten oxide (W₁₈O₄₉) nanowires on sputter-deposited W films prepared under different O₂/Ar flow rate ratios (OAFRRs) in the sputtering gas is reported. After

thermally annealing at 700 – 850 °C in N₂ ambient for 15 min, dense and well crystalline W₁₈O₄₉ (010) nanowires or nanobelts were obtained depending on the oxygen content in the sputtering gas. Experimental results show that the annealing temperature required for the full growth of W₁₈O₄₉ nanowires reduced when the O₂/Ar flow rate ratios (OAFRR) in the sputtering gas was increased. It is found that the oxygen absorbed in the surface region is responsible for the growth of nanowires. As the OAFRR was increased to (8 sccm)/(24 sccm), which resulted in a saturated oxygen content of about 55 at.% inside the W film, large-scale nanobelts or nanosheets of W₁₈O₄₉ were grown. The possible growth mechanism which governs the evolution from nanowires to nanobelts as the O₂/Ar flow rate ratios (OAFRR) was changed is also discussed.

4.1.5 Thermal assisted spray

Liao et al [36] have used a spray-pyrolysis like process assisted with a thermal decomposition of tungsten oxide powder to synthesize nanowires of tungsten oxide. These WO_{3-δ} nanowires were grown directly from tungsten trioxide powder (99.9%) under controlled conditions without the presence of catalyst. The micrometric powder was placed at the center of a silica tube inserted in the horizontal tube furnace while the substrate was located out of the silica tube, where the temperature gradient, pressure and evaporation time were controlled. During the heating of the powder at about 950°C, the vapor was carried onto the substrate placed at the downstream end of the silica tube under a mixed oxygen-argon atmosphere. The growth rate of the WO_{3-δ} nanorods is small at the order of 0.2 nm/s. It was shown that after electrochromic cycling above 1000 times, the nanowires synthesized by this method start to agglomerate in particular the parts immersed in the electrolyte.

4.1.6 Direct powder heating

Liao et al [37] have used a direct method to fabricate tungsten oxide ($\text{WO}_{3-\delta}$) nanowires for electrochromic devices applications. The $\text{WO}_{3-\delta}$ nanowires are grown directly from tungsten oxide powders in a tube furnace. The $\text{WO}_{3-\delta}$ nanowires have diameters ranging from 30 to 70 nm and lengths up to several micrometers. The $\text{WO}_{3-\delta}$ nanowires based device has short bleach-coloration transition time and can be grown on a large scale directly onto an ITO-coated glass that makes it a potential in many electrochromic applications. The structure, morphology, and composition of the $\text{WO}_{3-\delta}$ nanowires were characterized using X-Ray diffraction and Raman spectroscopy. It was found that the $\text{WO}_{3-\delta}$ nanowires were exhibiting a net sub-stoichiometric phase, namely $\text{WO}_{2.9}$.

4.1.7 Vapor transport method

Tungsten oxide nanorods were grown by vapour transport from a WO_3 layer onto a substrate (Mica) in air at atmospheric pressure by Gillet et al [38]. The tungsten oxide vapors are produced by a WO_3 layer previously deposited on a SiO_2 slide and condensed onto a mica substrate. In this process, during the experiments the temperature difference between the substrate and the heated WO_3 layer determine the supersaturation and the condensation rate. In this work of Gillet et al, the working temperatures were fixed at 550 °C and 450 °C. After cooling down to room temperature, the surface of the mica substrates exhibited a series of in-plane oriented WO_3 nanorods.

CHAPTER FIVE

5.1 GROWTH MECHANISMS OF WO_{3-x} NANO-RODS STRUCTURES

5.1.1 Standard growth models:

Nanostructures including tungsten oxide produced by vacuum technologies on crystalline substrates are subject to numerous mechanisms during their growth. This applied to thermal evaporation in particular which is carried out by placing the substrate in a vacuum chamber facing the target and hitting it with beams of evaporated material from heated effusion containers. After atoms and molecules strike the substrate surface, several processes are possible as they are incorporate into the crystal. These surface processes are affected by the composition and physical properties of the participating materials and consequently, are temperature dependent. The major thermodynamic phenomena which could be observed during a thermal evaporation process, and as shown in Figure 13, are:

- (i) Migration process,
- (ii) Adsorption phenomena,
- (iii) Desorption process,
- (iv) Interdiffusion,
- (v) Incorporation or implantation processes.

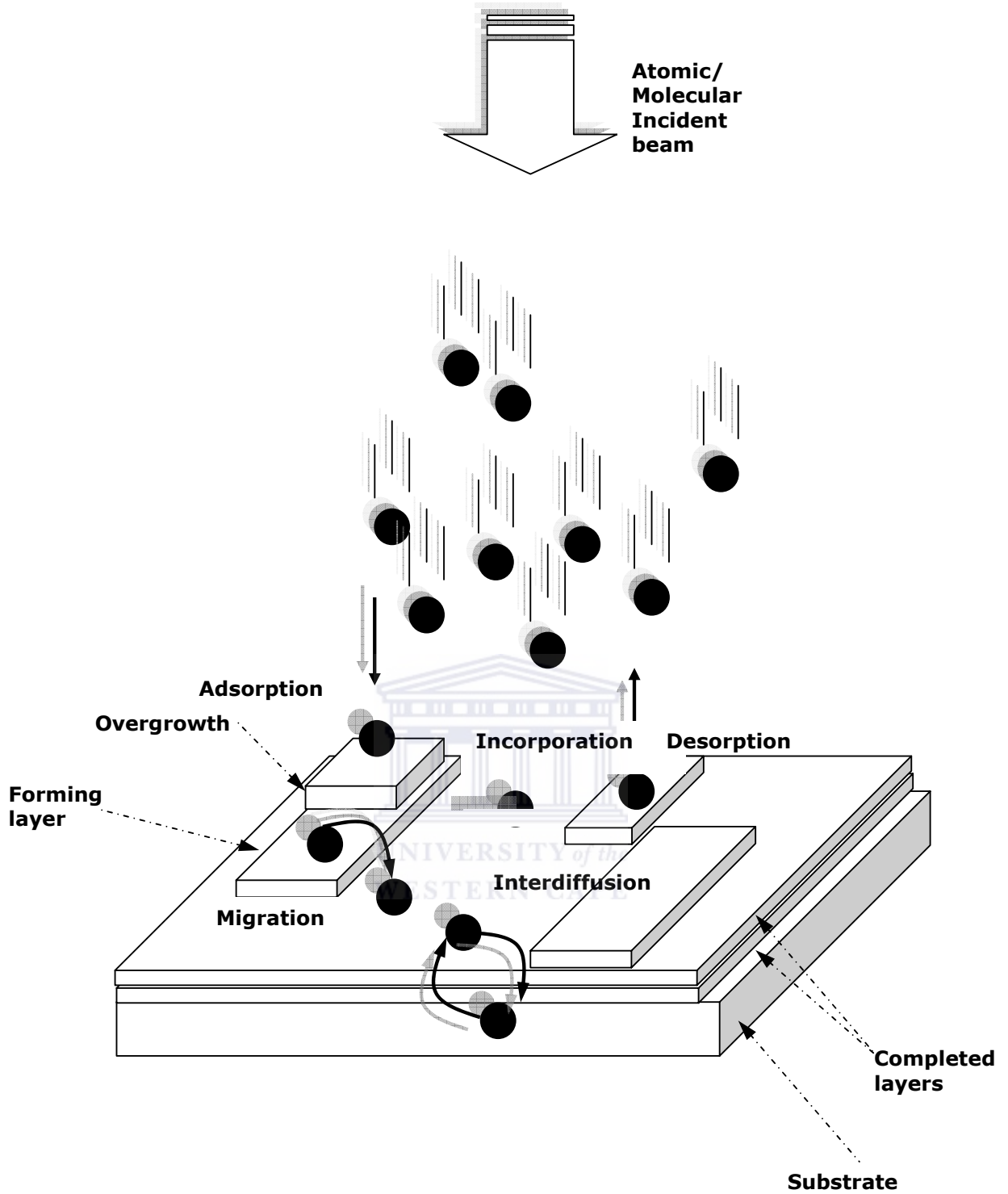
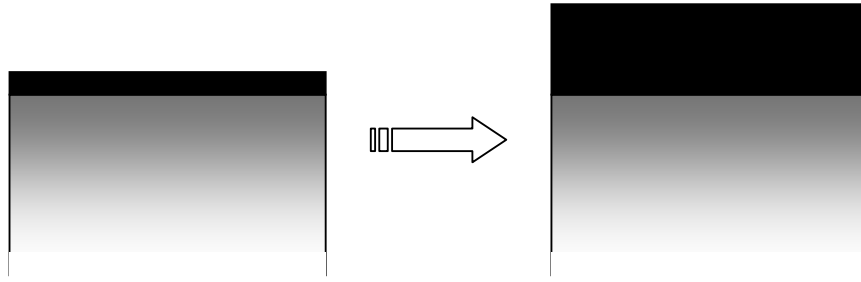
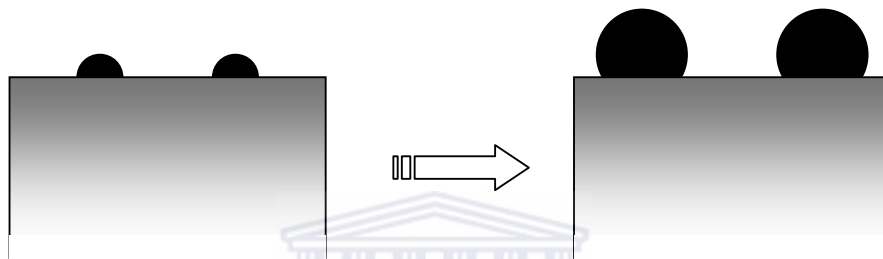


FIGURE 13
 Ionic and charge exchanges mechanisms in a WO_3 based electrochromic window.

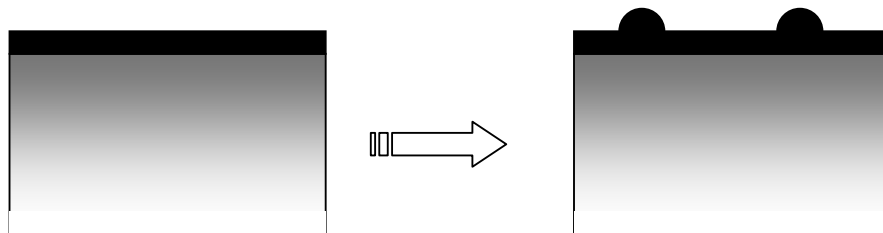
During the growth of any nano-structure in particular if it is an epitaxial one, there are three possible modes as shown in Figure 14. The first, Frank-van der Merwe, is simply the successive addition of 2-dimensional atomic layers to the substrate. The second one, Volmer-Weber, will occur if the added material can minimize its free energy by trading increased surface area for decreased interface area, forming an island structure like water droplets on glass. A third possibility can arise if the lattice spacing of the added material mismatches the substrate. Here the growth starts with a 2-dimensional strained wetting layer, but islands form after the first few atomic monolayers. The driving force is the incorporation of dislocations within the islands to relieve the strain. This third mode is called Stranski-Krastanow mode. A variation on the Stranski-Krastanow mode is found in Ge on Si. In this system, after the first 3-6 monolayers form a wetting layer, islands form. However no misfit dislocations are present in these islands Chen et al [35]. The proposed mechanism allowing this structure is elastic deformation of the substrate and island to lower the strain energy. This mode is called coherent Stranski-Krastanow growth. The island shapes predicted from this particular growth mode assume that the atoms are in their most thermodynamically favorable arrangement. However adsorbed atoms are unlikely to reach the most favorable spot before being covered with new atoms, especially when growing at high rates or low temperatures. Evidence suggests that the so called “hut” shaped clusters are a metastable intermediate in the formation of islands. Alternative pathways to island formation are possible, resulting in variation of the final island structure such as the nano-structured elongated rods with clear shape anisotropy.



Frank-van der Merwe



Volmer-Weber



Stranski-Krastanow

FIGURE 14

Main growth mechanism modes (a) Frank-van der Merwe, (b) Volmer-Weber and (c) Stranski-Krastanow.

5.1.2 Vapor-Liquid-solid single crystal growth mechanism of nanorods structures

The mechanism of single crystal growth from a vapor has been described by Wagner and Ellis [39]. In this mechanism an impurity is described as an important factor for the silicon whisker growth, whereby the role of an impurity is to form a liquid alloy droplet of relatively low freezing temperature. The liquid droplet is the most preferred site for deposition from the vapor, which causes the liquid to become supersaturated with Si. The whisker grows by precipitation of Si from the droplet. Wagner and Ellis as described in their paper, considered Au as an impurity for growing whiskers of Si. A small particle of Au is placed on a (111) surface of a silicon wafer and heated to 950°C, forming a small droplet of an Au-Si alloy. The liquid alloy acts as a preferred sink for arriving Si atoms or likely as a catalyst for the chemical reaction involved. The Si enters the liquid and freezes, with a very small concentration of Au in solid solution, at the interface between a solid Si and the liquid alloy. As a result of the continuation of this process, the alloy droplet is displaced from the substance crystal. The growth direction is $\langle 111 \rangle$, and the side faces of the whiskers are usually (211) but sometimes (211) and (110). The whisker grows in length by the VLS mechanism until the growth conditions are changed. Vapor-Liquid-Solid growth of Si whisker can occur over a wide range of cross-sectional dimensions. The selection of a good impurity for VLS growth depends on a number of factors such as formation of a liquid alloy at the deposition temperature, Vapor-Liquid-Solid interfacial energies, distribution coefficient and inertness to the reaction product.

CHAPTER SIX

6. EXPERIMENTS AND EXPERIMENTAL RESULTS

6.1 Synthesis and Characterization

Following to the survey of chapter 4 and due to its simplicity, the method of Liu et al has been used extensively within the framework of this research work [33]. A spiral coil of 1 cm in diameter and ~10cm in length was made with a tungsten wire (Aldrich chemical Comp) of a high purity 99.995% and connected to two copper electrodes in the evaporator vacuum chamber [Figure 15]. A series of planar substrates of Si(100) and mica as well as corning glass (10x10x ~1mm³) were used. The distance tungsten wire to substrate was fixed at 50 mm and 100 mm. Before evaporation, the substrates were ultrasonically cleaned in acetone, alcohol and deionized water in sequence (for 20 minutes each phase) and were fixed on a substrate holder ~50 mm above the coil. The vacuum chamber was first pumped down to $\sim 3 \times 10^{-2}$ mbar, and then an adjusted voltage was applied to the two copper electrodes, generating a current through the tungsten coil, rapidly heating up the coil. The current was varied in the range of 8-13.5A instead of 45-50A as in the case of Liu et al. The deposition time under an oxygen atmosphere was varied from 1 min to 15 minutes. The coil temperature was monitored at a distance of ~1 m approximately with an IR radiophotometer-viewer (Kane May Instrumentation Infratrace 2000). The advantage of this synthesis method is the easy control of the nanorods' growth via adjusting the voltage applied to the two electrodes or, equivalently, the current passing through the coil. When passing a current of about 13 A through the tungsten coil for approximately ~1 min, large scale-tungsten oxide nanorods have been deposited on all substrates used. The temperature

of the coil, as monitored by the IR radiophotometer, the measured temperature was 950°C. The pumping system consisted of a rotary and turbo-molecular pump. When all the pumps were working, the evaporation chamber reached a base pressure of about 4×10^{-5} mbar. Before any evaporation, the tungsten filament was outgassed for ~30 minutes, to remove any impurities not required in the deposits. A small amount of air was introduced into the system and subsequently reached the desired operating pressure of 4×10^{-2} mbar. While the studies were conducted mainly on the as grown tungsten oxide samples, a series of samples was heated to investigate the thermal treatment in oxygen enriched atmosphere on the characteristics of the as-grown nano-rods if any. The annealing has been performed using a Lindberg tube-type furnace with a temperature control in oxygen atmosphere [Figure 16]. Selected samples on Si(001) were annealed in the range of 400- 645°C each for 2 hours.

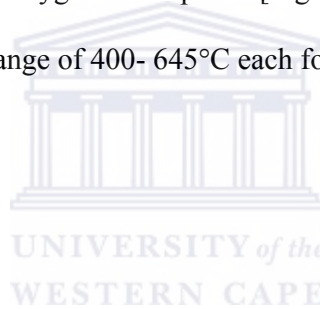




FIGURE 15
Thermal evaporator used for the synthesis of the $\text{WO}_{3-\delta}$ nanorods onto mica, Si(001) and Corning glass ultra-sonicated substrates.



FIGURE 16

Lindberg-horizontal tube type furnace used for the samples' heating in an oxygen rich atmosphere.

6.1.1 Morphological investigations by scanning electron microscopy

To study the shape anisotropy of the as grown nanostructured tungsten oxide, high resolution electron microscopy was used as a primary characterization tool. The Scanning Electron Microscope used in this study was a Stereo Scan 440, the beam energy used was 20kV.

Figure 17 shows a typical scanning electron micrograph of typical tungsten oxide deposited onto ultra-sonicated mica, corning glass and Si(001) substrates at early stages of the growth corresponding to a deposition time of ~5 min. One can distinguish clearly the formation of the nanoparticles of the tungsten oxide with significant shape anisotropy: nanorods on the three substrates. The density of these tungsten oxide nanorods is high in the case of Si(001) while low for mica and corning glass substrates. Compared to the nanorods grown on Si(001), the nanorods onto mica and corning glass exhibit sharp edged crystallites. In addition, they seem to prefer a spatial orientation parallel to the surface of mica and glass. The nanorods are larger both in transversal as well as in the longitudinal direction in the case of mica. Their longitudinal average size can be as over 7 μm and 3 μm on mica and glass respectively being still nano-scaled in the transversal direction. By contrast, the tungsten nanorods grown onto Si(001) are rather cylindrical in shape and exhibit a perpendicular spatial orientation to the substrate. They are rather agglomerated in bundles-like structure. While their longitudinal dimension can not be easily quantified, their basal diameter seems to be ≤ 450 nm in average.

In addition, Figure 17 indicates the existence of a disordered non continuous layer with the nanorods in both mica and corning glass substrates. This layer could correspond to the first deposits during the very early stages of nucleation of tungsten oxide.

To identify the importance of the nucleation phase for the growth of the observed tungsten oxide nanorods, evaporation on ultra-sonicated and non sonicated substrates were done during ~8 min. Indeed, in addition to the nature of the substrate, another factor that influences the growth of the tungsten oxide nanorods is the cleanliness of the substrate itself. While the cleanliness of Si (001) and cleaved Mica substrates were not critical, the surface quality of the corning glass substrates was decisive. Figure 18 shows scanning electron micrographs of tungsten oxide coatings grown on ultra-sonically non cleaned and cleaned corning glass substrates. Both depositions were made without heating the substrate at a fixed distance of 100 mm (distance tungsten wire-substrate). As it can be observed, while the tungsten oxide coating on the cleaned substrate exhibits the expected nanorods forms (not oriented spatially), the non-cleaned substrate coating presents an open and a complex morphology without any define shape anisotropy.

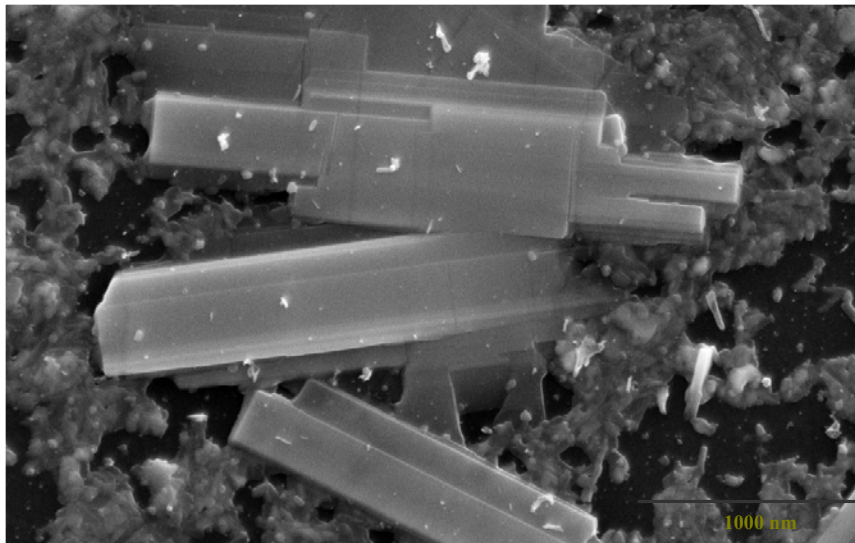
We also note the effect of the target-substrate distance which is 100mm instead the standard value of 50 mm. The as grown nanorods are thinner than those deposited at 50 mm. Their average basal size was observed at about 500nm.

In view of the different scanning electron microscopy observations, it can be observed that the tungsten oxide nanorods deposited on mica, in addition to their preferential orientations which could be due to the cleaved mica edges, seem to grow parallel to

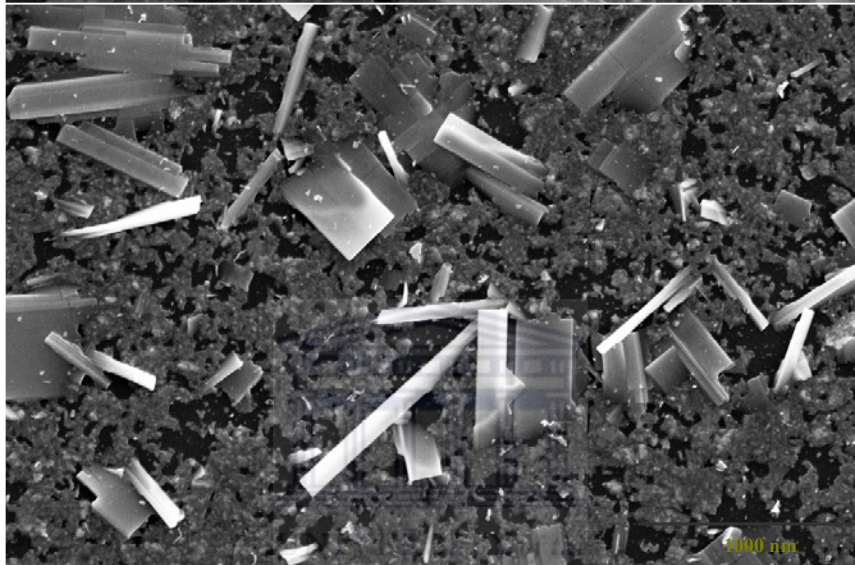
the substrate in particular for short depositions as reported in Figure 19(a). These peculiar planar orientations of the nanorods onto mica should be correlated to a possible epitaxial growth process. A possible explanation of this particular growth on mica is proposed in the following section.



**(a) Mica
substrate**



**(b) Glass
substrate**



**(c) Si(001)
substrate**

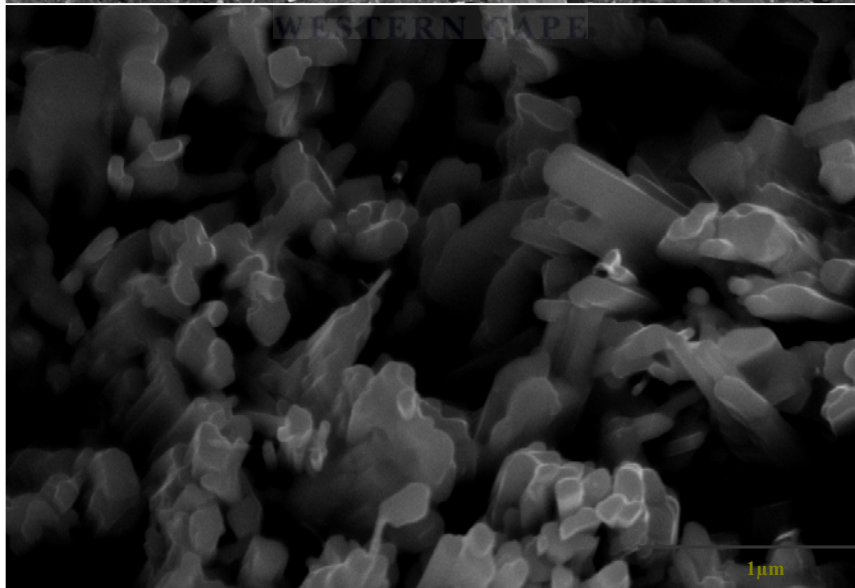
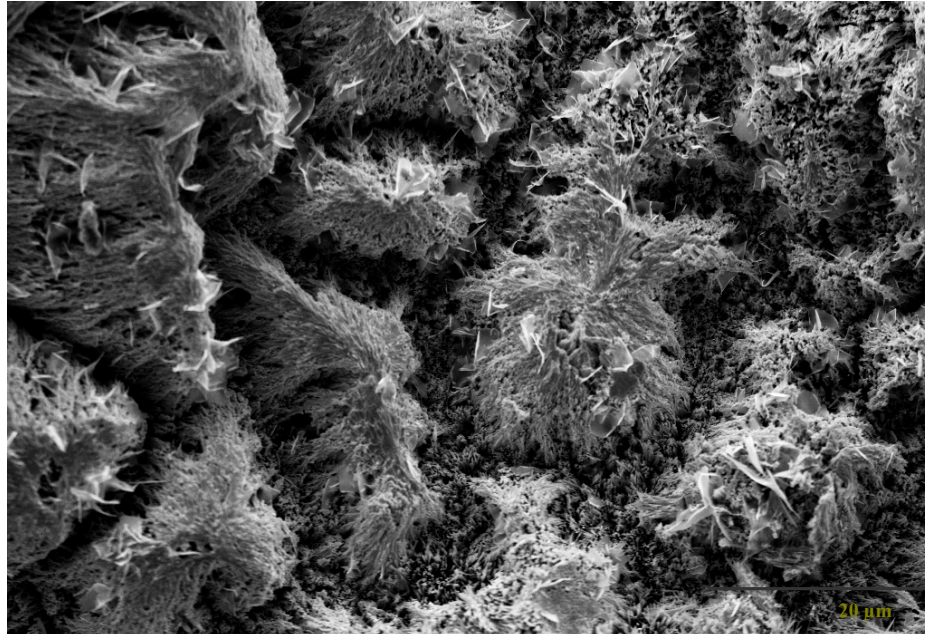


FIGURE 17

Scanning electron micrographs of WO_{3-δ} nanorods on different substrates at early stage of growth

(a)



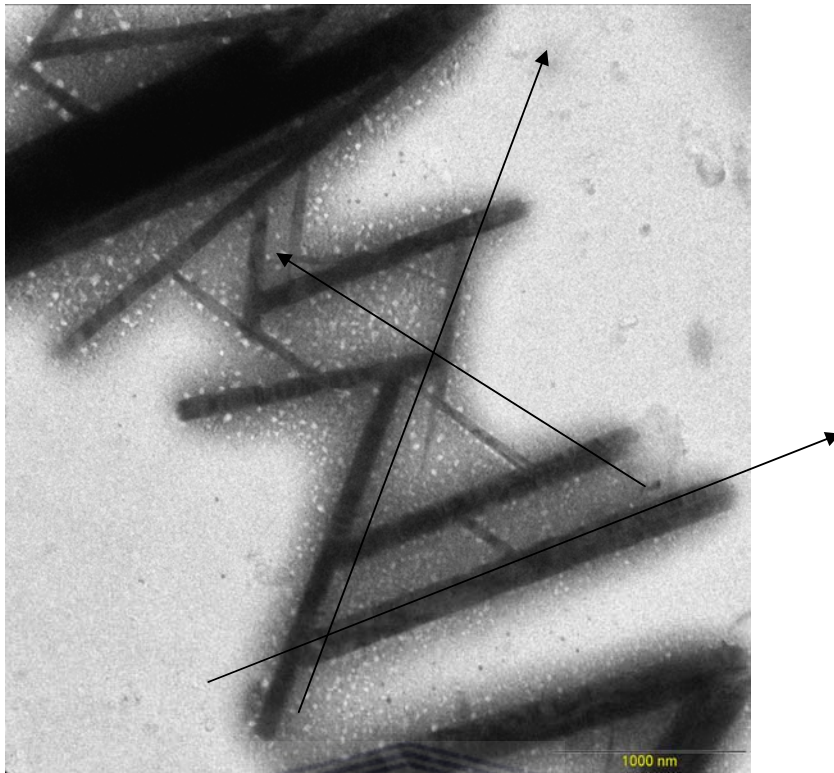
(b)



FIGURE 18

Influence of surface cleanliness on the texture of the deposited tungsten oxide coatings onto ultrasonically (a) non cleaned and (b) cleaned corning glass substrates.

(a)



(b)

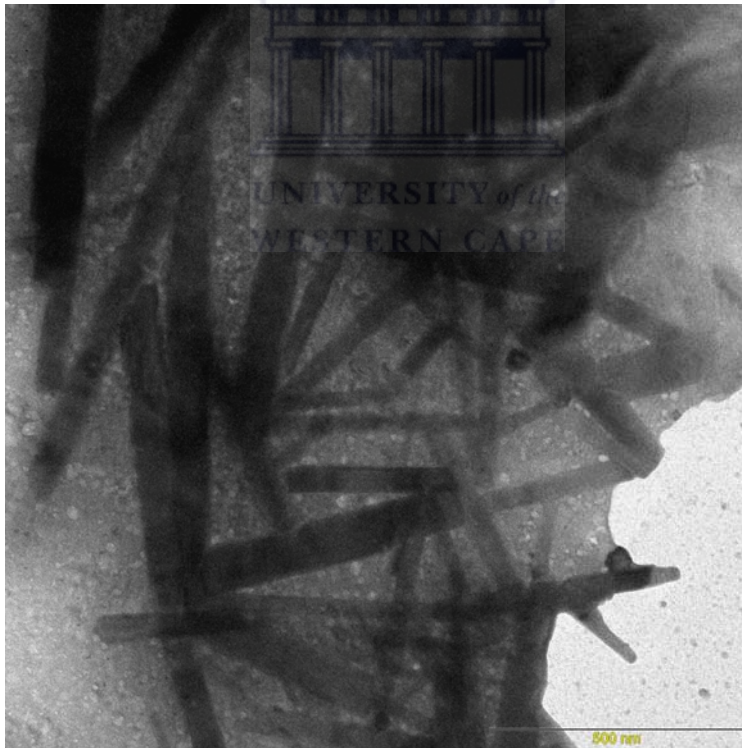


FIGURE 19

Scanning electron micrographs of tungsten oxide nanorods deposited for (a) 1 min (b) 5 min both on mica at a distance tungsten wire to substrate of 100 mm.

6.1.2 Mechanism of growth and orientation on Mica substrates

As mentioned previously, relatively to Si(001) and Corning glass substrates, the tungsten oxide nanorods deposited onto mica exhibit a certain degree of planar preferential growth. This distinctive growth ordering was reported earlier by Gillet et al [38]. In addition to this growth order, the nanorods present quasi constant angles between them of about: ~ 30 and ~ 45 deg. Excluding this angular orientation which will be discussed later, the specific growth behavior on mica could be from the same origin as in the case of the Gillet's research work in which the presence of potassium ions in mica plays a major role. It is known that in hydrated rich atmosphere and high temperature, tungsten oxide may be volatilized through the formation of $\text{WO}_2(\text{OH})_2$ according to the reaction $[\text{WO}_3 + \text{H}_2\text{O} \Rightarrow \text{WO}_2(\text{OH})_2]$. As in the case of Gillet et al, it is supposed that $\text{WO}_2(\text{OH})_2$ would be condensed on the mica substrate maintained at a relatively low temperature. In the first stage of growth $\text{WO}_2(\text{OH})_2$ reacts with the K ions of the mica surface giving a tungsten bronze following the reaction: $[\text{WO}_2(\text{OH})_2 + x\text{K} \Rightarrow \text{K}_x\text{WO}_3 + \text{H}_2\text{O}]$. In further growth stage WO_3 is condensed on K_xWO_3 . In the potassium tungsten oxide bronze K_xWO_3 , the W atoms are octahedrally coordinated with oxygen atoms to form WO_6 octahedrons. The WO_6 octahedrons join each other by sharing O corner atoms [Figure 20]. Tungsten bronzes can adopt various types of structures depending on the ionic radius of the incorporated metal atom and on the composition. Hexagonal tungsten bronzes can be formed with K ions in the composition range $0.13 < x < 0.33$. In these hexagonal bronzes, the WO_6 octahedrons form hexagonal tunnels where K ions can be located [Figure 20]. An epitaxial hexagonal tungsten bronze grows on the surface of the mica substrate and acts as a precursor for the further WO_3 nanorods growth. The resulting monoclinic

WO_3 structure results either on the growth of WO_3 on the hexagonal tungsten bronze or on the growth of a hexagonal WO_3 followed by the transition of the hexagonal structure to a monoclinic structure. Hexagonal tungsten oxide is a metastable phase and transforms irreversibly into the monoclinic structure WO_3 . This transformation has been studied in detail by Figlarz [41]. Hence, in the case of the current experimental nanorods of tungsten oxide onto mica, the tungsten bronze is likely to form an intermediate compound between the substrate and the WO_3 nanorods. This interfacial compound is responsible for the nanostructure orientations on the mica substrate. Assuming that “x” varies in a range of 0.4 to 0.6 and that the interfacial compound is a tetragonal tungsten bronze with lattice parameter $a = 12.3 \text{ \AA}$ and $c = 3.8 \text{ \AA}$ [42-43], Figure 20 represents such a configuration. In the (001) plane of the tungsten bronze, the next neighbour K atoms distance is about 0.47 nm which is approximately the distance between the K ions in the direction [210] on the mica surface. So during the first stage of the growth a tetragonal tungsten bronze is epitaxially formed with good accommodation as indicated in Figure 21. One can see that if a_{1s} , a_{2s} and a_{3s} are the distances of K atoms on the mica substrate in the directions [210], [230] and [130] respectively and a_d the distance of K atoms in the tetragonal tungsten bronze, the interfacial tungsten bronze accommodates the substrate with the following relations $a_{1s} = 2 a_d$, $a_{2s} = 3 a_d$ and $a_{3s} = 4 a_d$ according to the three directions [210], [230] and [130] so that the angles between the epitaxial orientations are in a good agreement with the experimental observations of the orientations of the synthesized tungsten nanorods on mica.

As mentioned before, In addition to this growth order, the nanorods present quasi constant angles between them of about: ~ 30 and ~ 45 deg. As this intrinsic

configuration was observed only on cleaved mica, this angular related phenomenon can be explained by steps that have been created during the cleavage phase. This cleavage operation was automatically conducted to have fresh surfaces of mica before each deposition.

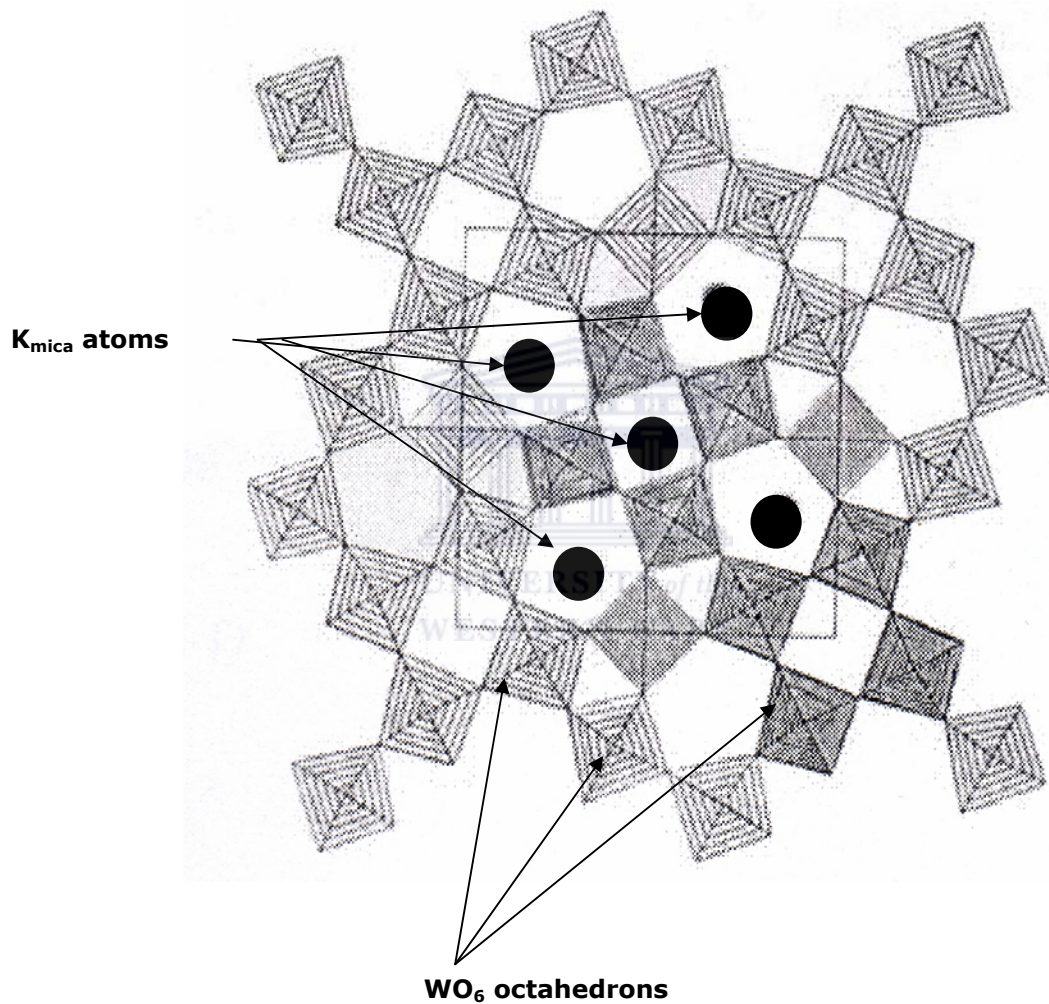


FIGURE 20
Schematic representation of (001) plane of the tetragonal tungsten bronze K_xWO_3
($0.4 < x < 0.6$), $a = 1.23 \text{ nm}$, $c = 0.38 \text{ nm}$.

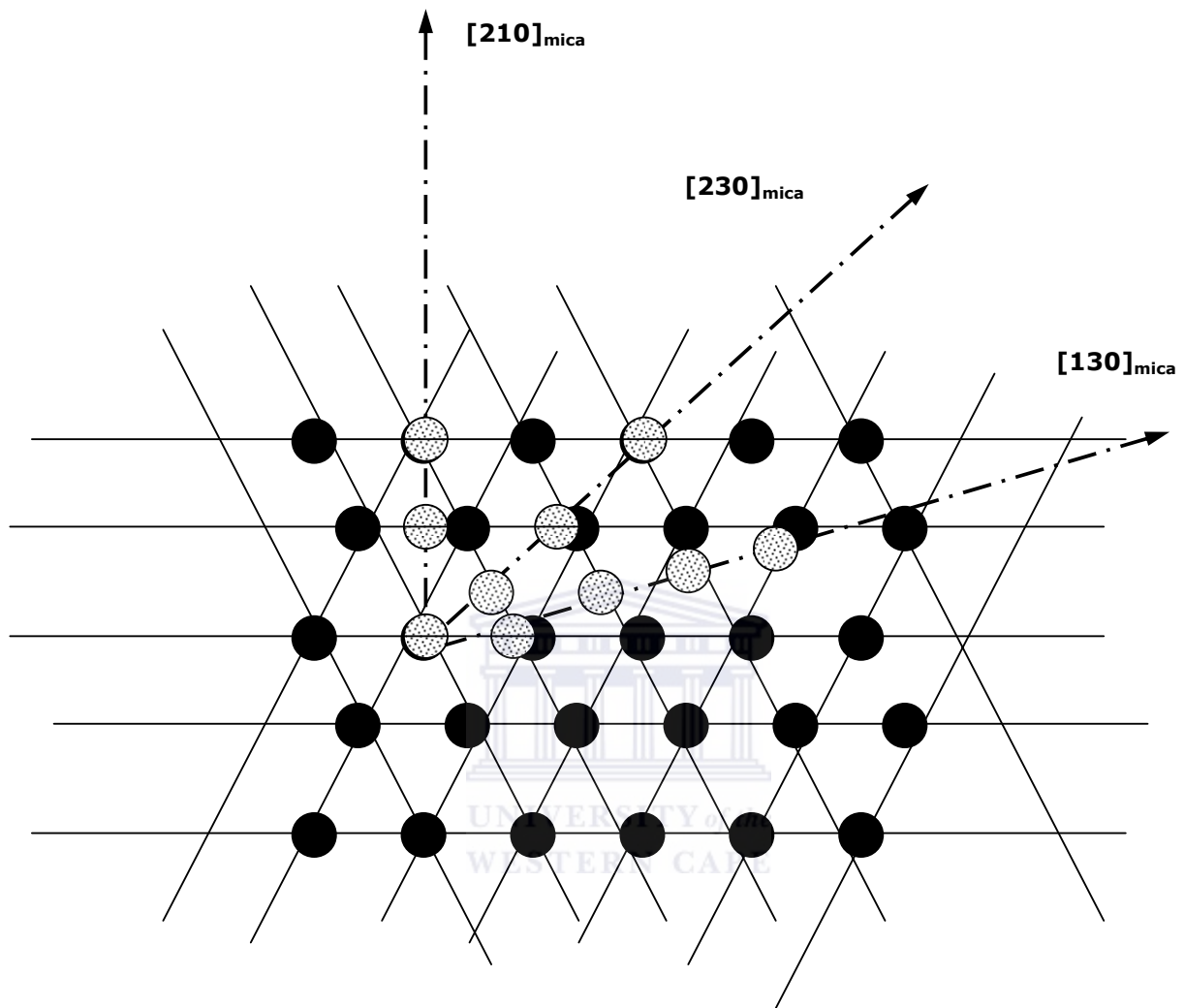


FIGURE 21
 Growth stage of tetragonal tungsten bronze K_xWO_3
 ($0.4 < x < 0.6$), $a = 1.23$ nm, $c = 0.38$ nm.

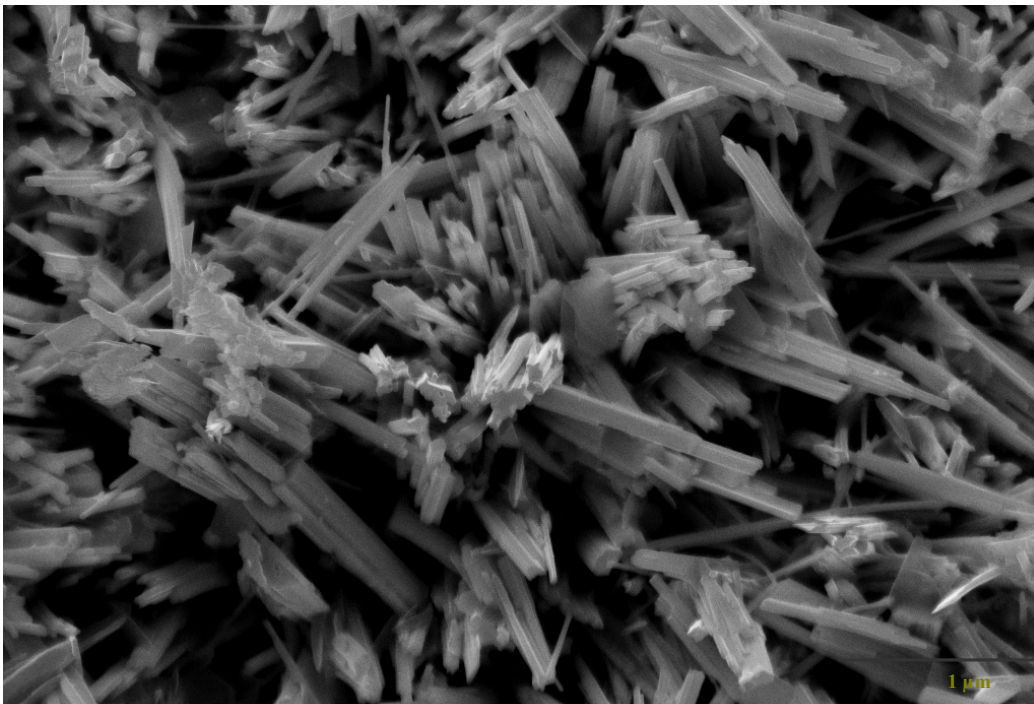
6.1.3 Mechanism of growth and orientation on Si(001) substrates

It is observed experimentally that the tungsten oxide nanorods deposited onto mica are oriented within the basal plane while they are isotropically oriented in the case of corning glass substrates as reported in Figures 17 and 19. This behavior is consistent independently from the duration of deposition as well as the heating temperature. Therefore, as suggested previously, the plausible explanation of such configurations should be correlated to the crystalline and amorphous states of the mica and glass substrates respectively. The significant degree of orientation of the nanorods transversally to the Si(001) substrates could be related to the specific mode of growth called the vapor-liquid-solid (VLS) mechanism on oriented semiconductors generally. This VLS crystal growth mechanism was proposed by Wagner and Ellis in 1964 for silicon whisker growth [39,44] and has been extensively used to guide the growth of various kinds of 1-dimensional nanostructures such as Ni doped GaP nanowhiskers onto (111) GaP [45]. In this context, it is suggested that the initial clusters of tungsten oxide are doped by Si which is caused by a diffusion process and in which these clusters act as catalysts for the pure tungsten oxide nanorods as in the case of mica. It is reasonable to expect that the growth temperature of about 700 - 850°C in an oxygen rich atmosphere within the vacuum chamber, tiny droplets of low melting point liquid containing W, O and Si are produced from the oxidation of W and diffusion of Si at the interface of oxidized tungsten liquid droplets. These possible tiny droplets reaching the supersaturating state would act as the seeds or templates for the nanorods growth perpendicular to the Si(001) surface. In this proposed mechanism, the basal size of the nanorods should be directly related to the size of the initial droplet of

liquid. So the experimental conditions have to be carefully controlled to avoid the formation of large droplets of liquid.

In order to support the proposed mechanism explaining the observed nanorods growth type of tungsten oxide on Si(001), a series of experiments were performed. While keeping the Si(001) substrates unheated and oxygen flow constant, the filament current was changed from 8 to 13.5 A. Under such conditions, the rate of vaporization of tungsten increases with the current while the thermalization of tungsten and tungsten oxide clusters decreases. Hence the basal size of the nanorods specifically should increase. Figure 22 shows the surface morphology of the nanorods and a corresponding transversal scanning electron micrograph cut at the early stage of growth. The cross section indicates the columnar-type growth taking place early during the growth process at the interface Si-deposit. Figure 23 show the scanning electron micrograph of the surface images of the tungsten oxide nanorods grown at 8, 10 and 13.5 A. If the length of the nanorods can not be easily quantified, the basal dimension increases with the current; from 150 nm, 300 nm and 1 μm for 8, 10 and 13.5 A respectively. Combined with the columnar growth type, this trend in the basal size seems to sustain the VLS growth model in the case of Si(001) substrates.

(a)



(b)

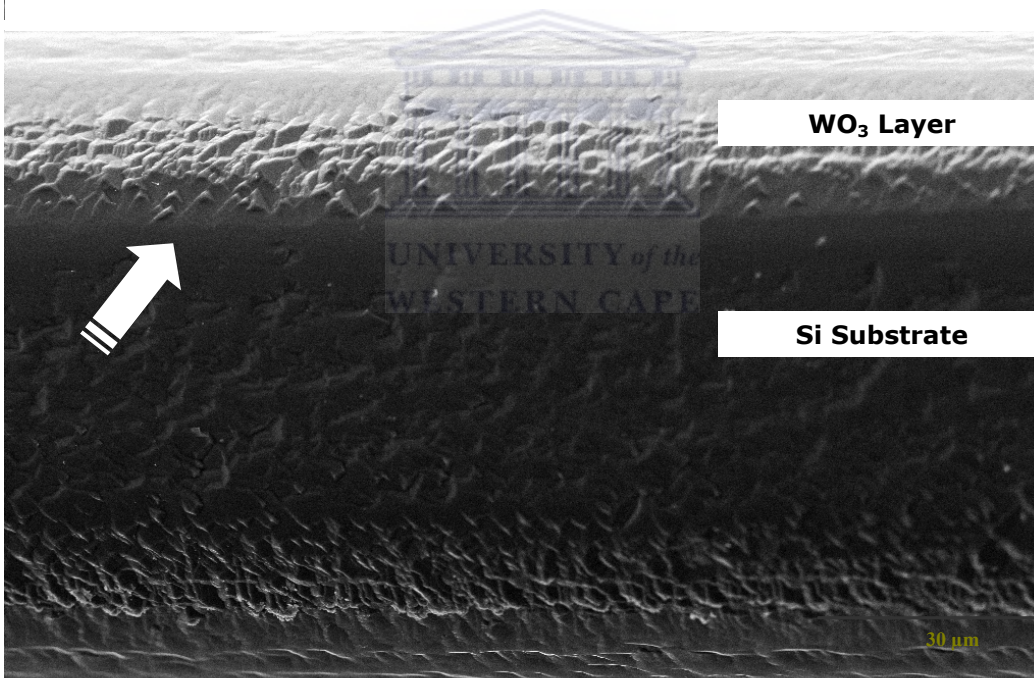
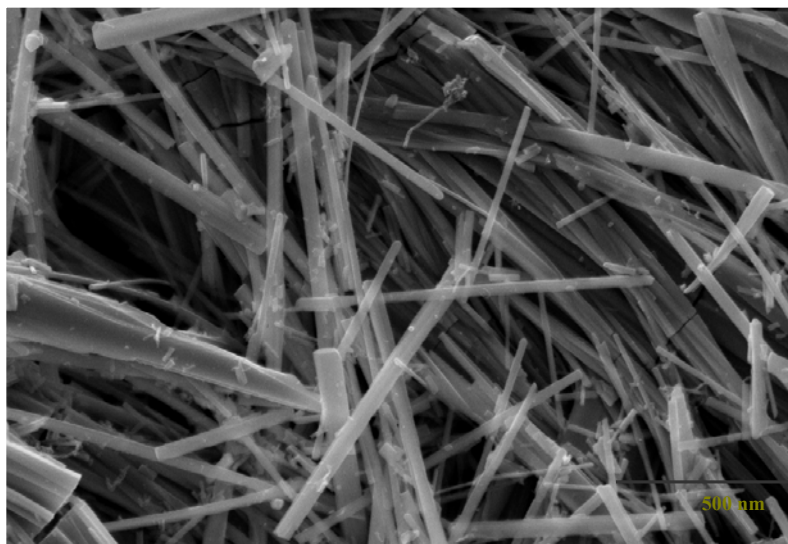


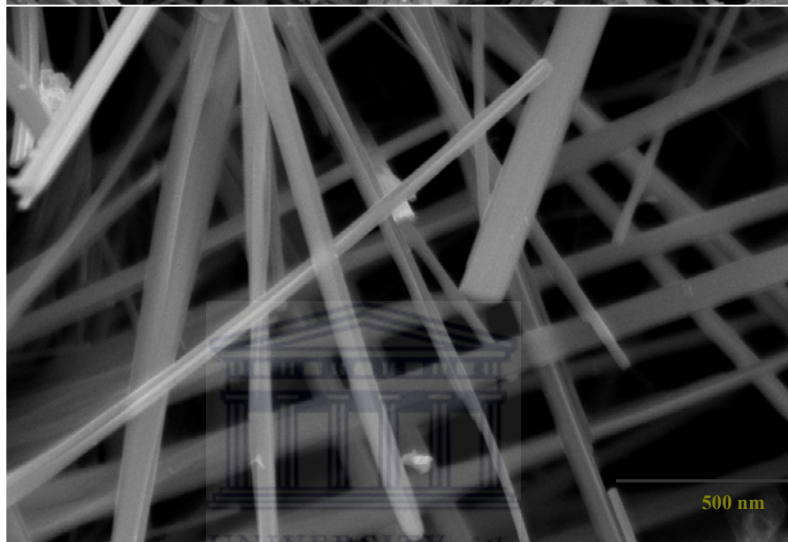
Figure 22

Scanning electron microscopy of tungsten oxide nanorods on (a) Si(100) substrate and (b) columnar growth structure on Si(100).

(a)



(b)



(c)

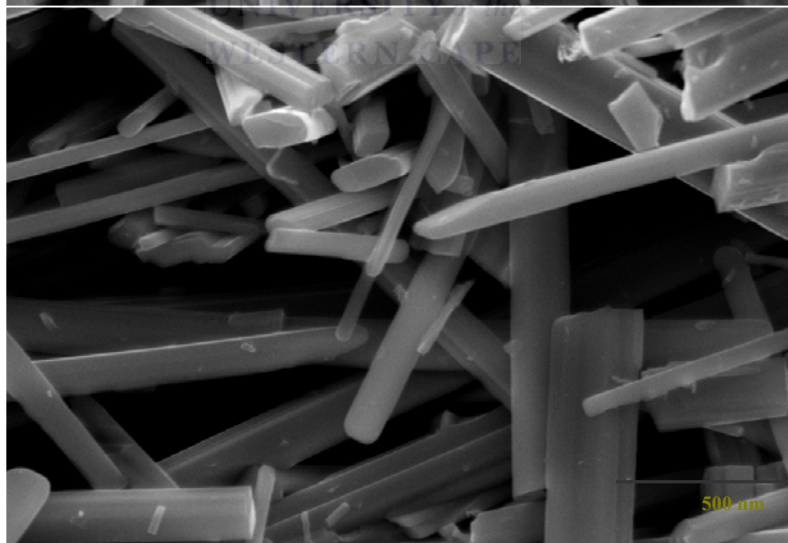


Figure 23

Scanning electron microscopy images of WO_{3-x} nanorods on Si(001) substrates for different currents (a) 8A, (b) 10A and (c) 13.5 A.

6.2 Chemical homogeneity of the tungsten oxide nanorods

As mentioned before, following the initial vacuum of about 4×10^{-5} mbar, before any evaporation, a small amount of air about $\sim 10\%$ relative to the initial vacuum system was introduced and subsequently reached the desired base pressure of 4×10^{-2} mbar. This was the optimum pressure used by Liu et al [33] in achieving quasi-stoichiometric tungsten oxide nanorods. To check the chemical homogeneity of the deposits on the substrates, more specifically in terms of tungsten and oxygen distribution all over the substrate, Electron Energy Loss Spectra (EELS) has been used. EELS is a micro-analytical technique that uses the characteristic spectrum of energy losses of transmitted electrons to obtain information about elemental composition, chemical bonding, and electronic structure. An EELS spectrum consists of a monotonically-decreasing background on which several broad peaks, each characteristic of a particular inelastic scattering process, are superimposed. The spatial resolution is limited by the diameter of the incident illumination focused on the sample. Due to the high energy spectral resolution, elemental information as well as molecular information can be detected. For such a purpose, a LEO type unit was used operating with a voltage of 100V and LaB6 as source. The allowed resolution is about 0.35 nm with a tilt range of $\pm 60^\circ$. For these measurements, the deposits which have had to be thin were removed from the mica substrates by immersion in de-ionized H₂O and then collected on standard carbon coated grids of copper.

Figure 24 depicts the EELS 2-D elemental imaging of both O and W corresponding to 1 min deposited tungsten oxide onto mica. We see clearly the high resemblance of the two elemental topographies. There is a high existence of homogeneous distribution of both O and W within the deposits and therefore a possible constancy of the ratio O/W

and hence the stoichiometry of the tungsten nanorods on the mica, corning glass and Si(001) substrates.

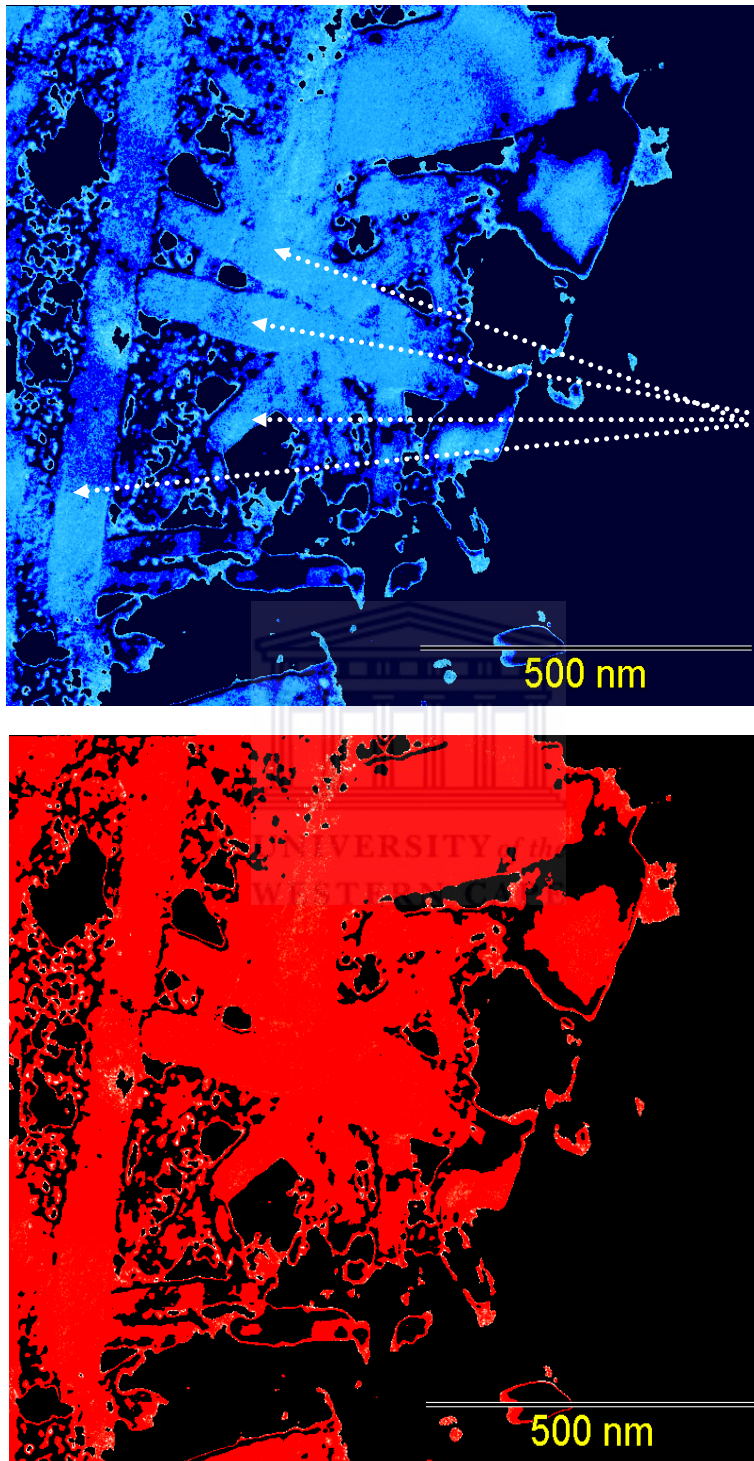


FIGURE 24

EELS mapping of deposits onto carbon coated grids tungsten (W: Blue) and oxygen (O: red).

6.3 Chemical stoichiometry and O/W ratio

From the literature survey, it appears obviously that any tungsten oxide nano-systems exhibiting a sharp anisotropy in shape such as nanorods, nanowires, nanoribbons, nanowhiskers do present inevitably a chemical sub-stoichiometry. The major observed phases are $WO_{2.9}$ and $W_{18}O_{49}$ with the hydrated $WO_3 \cdot H_2O$. Following the investigations by EELS which showed a priori a homogeneity in elemental distribution of W and O within the basal plane of the deposits, Rutherford Backscattering Spectrometry (RBS) has been used to quantify the elemental composition of the nanorods of tungsten oxide deposited on Si(001) and ultrasonically cleaned corning glass and mica substrates. The experiments were carried out on the Van de Graaf accelerator of iThemba LABS with 3.050 MeV $4He^+$ ions beam (Charge: 20.00 μC and current = 5.00 nA). The beam-target geometry characteristics were: $\theta = -10.00$ deg, $\phi = 15.00$ deg and $\psi = 5.00$ deg. The deposits on Si(001) were preferred as the corresponding RBS profiles are unmixed and simple to interpret at a certain extent. Figure 25 shows a typical experimental Rutherford Backscattering profile on Si(001) and its optimal simulation curve. The W, Si and O edges are localized at the following energy channels of 457, 279 and 178 respectively. In general, the simulated curves using the standard RUMP program do not fit perfectly the experimental ones. This difficulty in obtaining very good simulations is due to the open framework of the nanorods architecture as noted in the previous scanning electron micrographs and therefore can not be considered as a standard continuous atomic layered system anymore. Hence, the targeted elemental ratio W/O

which is of interest in this case should be primarily quantified for the dense nanorods coatings deposited on Si and corning glass substrates. The average experimental value of O/W is about 2.52 from the best simulated profiles which is by far lower than the stoichiometric WO_3 . Even if one considers an additional $\sim 10\%$ due to the intrinsic porosity of the nanorods deposits, the ratio O/W becomes 2.77, but still lower than 3. One could therefore conclude that the tungsten oxide nanorods deposits are sub-stoichiometric and would fit with either $\text{W}_{18}\text{O}_{49}$ (O/W ~ 2.72) or $\text{WO}_{2.9}$ (O/W = 2.9). These investigations in agreement with previous studies confirm that the significant shape anisotropy in the tungsten oxide systems is synonymous of a sub-stoichiometric tungsten oxide: $\text{WO}_{3-\delta}$.



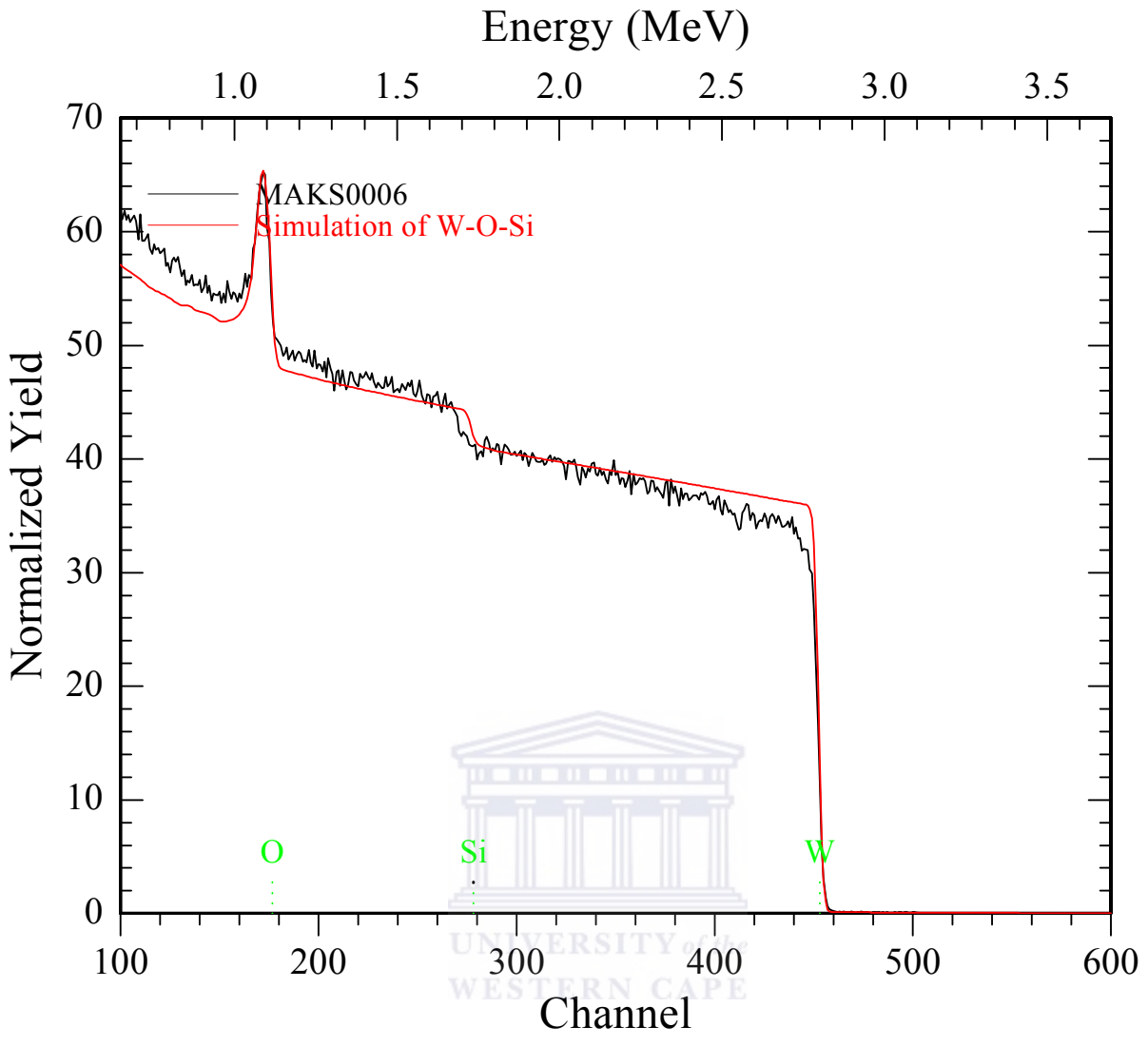


FIGURE 25
 Rutherford Backscattering profile of dense nanorods deposits on ultrasonically cleaned Si(001).

6.4 Vibrational properties and chemical stoichiometry

To confirm the previous sub-stoichiometric aspect of the synthesized $\text{WO}_{3-\delta}$ onto the different substrates, infrared spectroscopy investigations were carried out at room temperature. Indeed, any sub-stoichiometry should affect the vibrational properties induced by bonding and vibrational modes. The infrared transmittance measurements were acquired with a Perkin-Elmer Paragon 1000, equipped with a wide band MCT mid-IR detector connected to the FT-IR spectrophotometer. The IR measurements range were performed in the spectral range of $400\text{-}4000\text{ cm}^{-1}$. As a reference and guidance, standard bulk WO_3 was measured in identical conditions. The standard powder and the $\text{WO}_{3-\delta}$ nanorods removed from the substrates were mixed with potassium bromide (KBr) used as a binder. Figure 26 shows a representative infrared transmission of the $\text{WO}_{3-\delta}$ nanorods compared to the standard bulk sample's signature. They are similar in the range $1200\text{-}4000\text{ cm}^{-1}$ with certain specificities for the infrared signature of the $\text{WO}_{3-\delta}$ nanorods samples. This latter exhibit different trend in the spectral region of $400\text{-}1200\text{ cm}^{-1}$. As indicated in Figure 25, they show a large peak at $690\text{-}700\text{ cm}^{-1}$, which may be ascribed to stretching modes of W-O-W amorphous WO_3 or crystalline $\text{WO}_{2.9}$. As the synthesized nanorods are highly crystalline considering the specific sharp Bragg peak observed around $20\text{-}34.2$ in the X-ray diffraction pattern as it will be shown later, one could conclude that this W-O-W vibrational mode is proper to the substoichiometric $\text{WO}_{2.9}$ rather to amorphous WO_3 . Similarly, the nanorods show two peaks at 730 and 807 cm^{-1} . These two peaks could be ascribed to the stretching vibration of crystalline W-O which seems to corroborate with the previous X-ray diffraction patterns of the nanorods by Liu et al [33]. In addition, one should point out that all the spectra of the different $\text{WO}_{3-\delta}$

nanorods samples exhibited broad curvatures around $3400\text{-}3500\text{ cm}^{-1}$, which indicates O-H stretching modes. This could be related to adsorbed water molecules as the $\text{WO}_{3-\delta}$ nanorods samples do present a significant porosity and therefore a high reactive surface which might react with atmospheric water vapour.



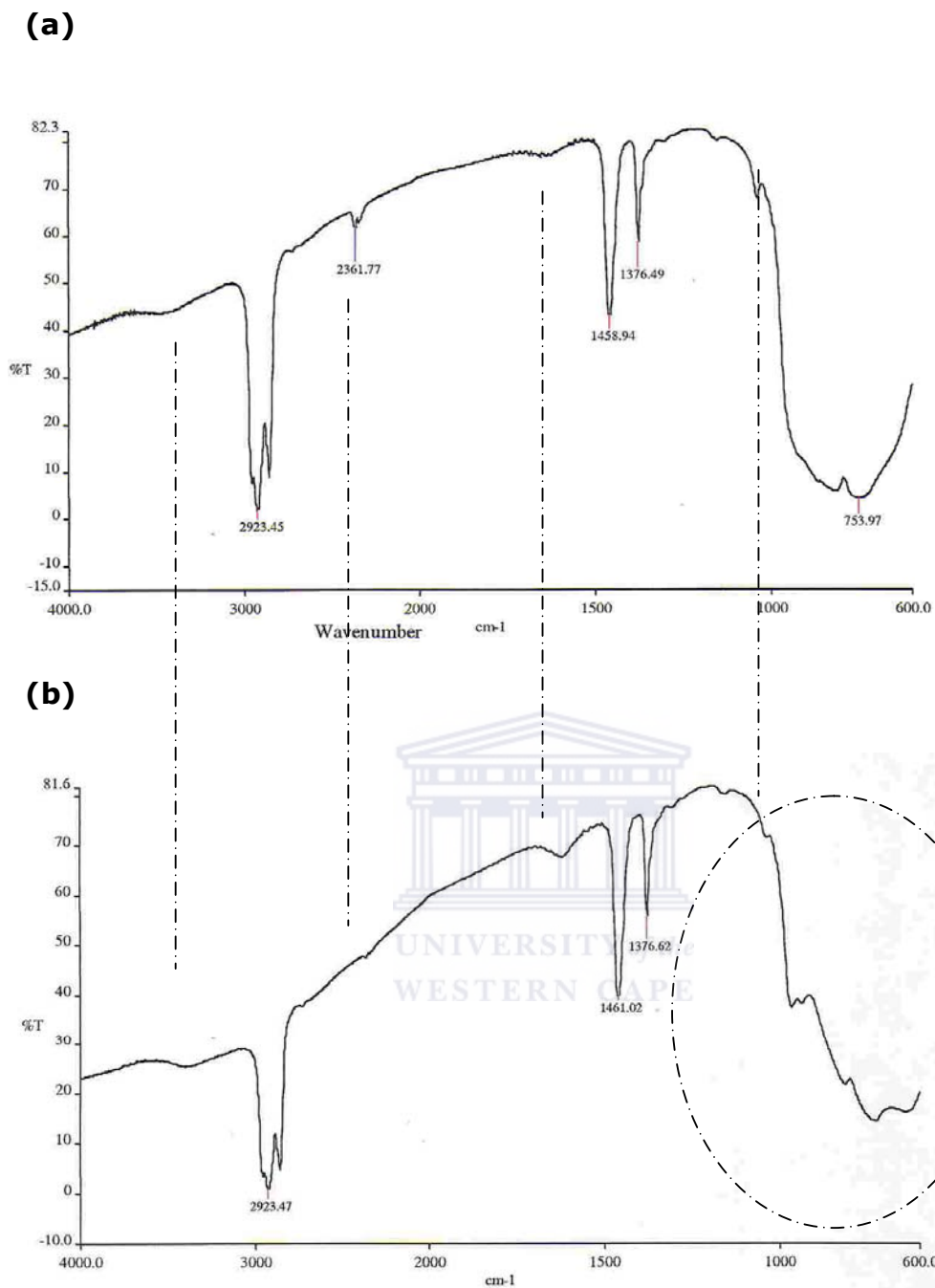


FIGURE 26

Room temperature Infrared spectroscopy profiles of (a) bulk WO_3 and (b) dense nano-rods deposits on $\text{Si}(001)$ substrate.

6.5 Crystallographic properties

The crystallographic structure of the tungsten oxide nanorods have been investigated using room temperature X-rays diffraction on a Brucker type unit in $\Theta-2\Theta$ scan mode. For pure comparison, standard stoichiometric powder (Johnson Matthey) was tested first as a guidance sample. Figure 27 shows its corresponding X-ray diffraction pattern which fits with the monoclinic phase, referenced as JCPDC card 5-363.

Figure 28 is a typical X-rays diffraction pattern of large array of nanorods taken with a step scan-angle of 0.02 deg, using the copper $K\alpha$ radiation (1.5405 Å). The pattern shows the general trend consisting of 2 wide Bragg peaks and 2 sharp peaks located at 23.12, 33.10 and 33.63, 33.69 deg respectively. The existence of the sharp peaks is in agreement with the sharp anisotropy of the nanorods. The large peak around 33.10 deg could be due to the very small grains located at the interface glass substrate-nanorods deposit. This hypothesis is advanced in view of the observation by scanning electron microscopy of Figure 24. The Bragg peaks located at 23.12, 33.63 and 33.69 do fit better with the JCPDC file 5-386 of $W_{20}O_{58}$ monoclinic structure i.e. in term of O/W is about 2.9. If so then the $W_{20}O_{58}$ nanorods are textured with a preferential orientation [312] instead of the [010]. Since no other significant diffraction peaks of the $W_{20}O_{58}$ ($WO_{2.9}$) phase were observed in the different pattern, one could conclude that their axis should be along [312] direction. In the case of the nanorods deposited on clean Si substrates, it is plausible to deduce that the oriented nanorods on Si substrates have their axis almost normal to the substrate, i.e. [312] $W_{20}O_{58}$ ($WO_{2.9}$) nanorods parallel to $[001]_{Si}$.

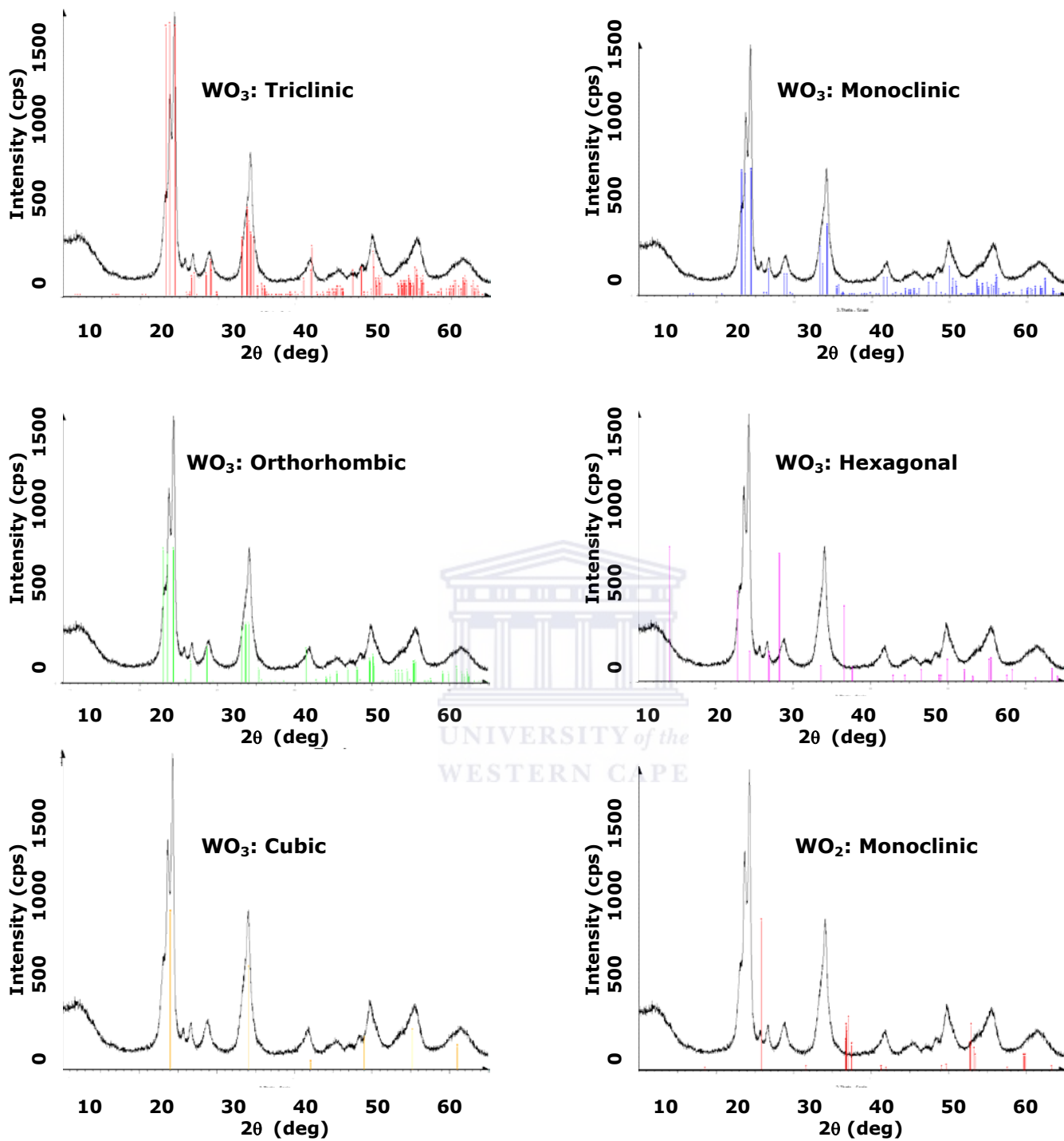


FIGURE 27

Room temperature XRD profile of the standard WO₃ powder used as a reference and the possible simulated crystalline phases.

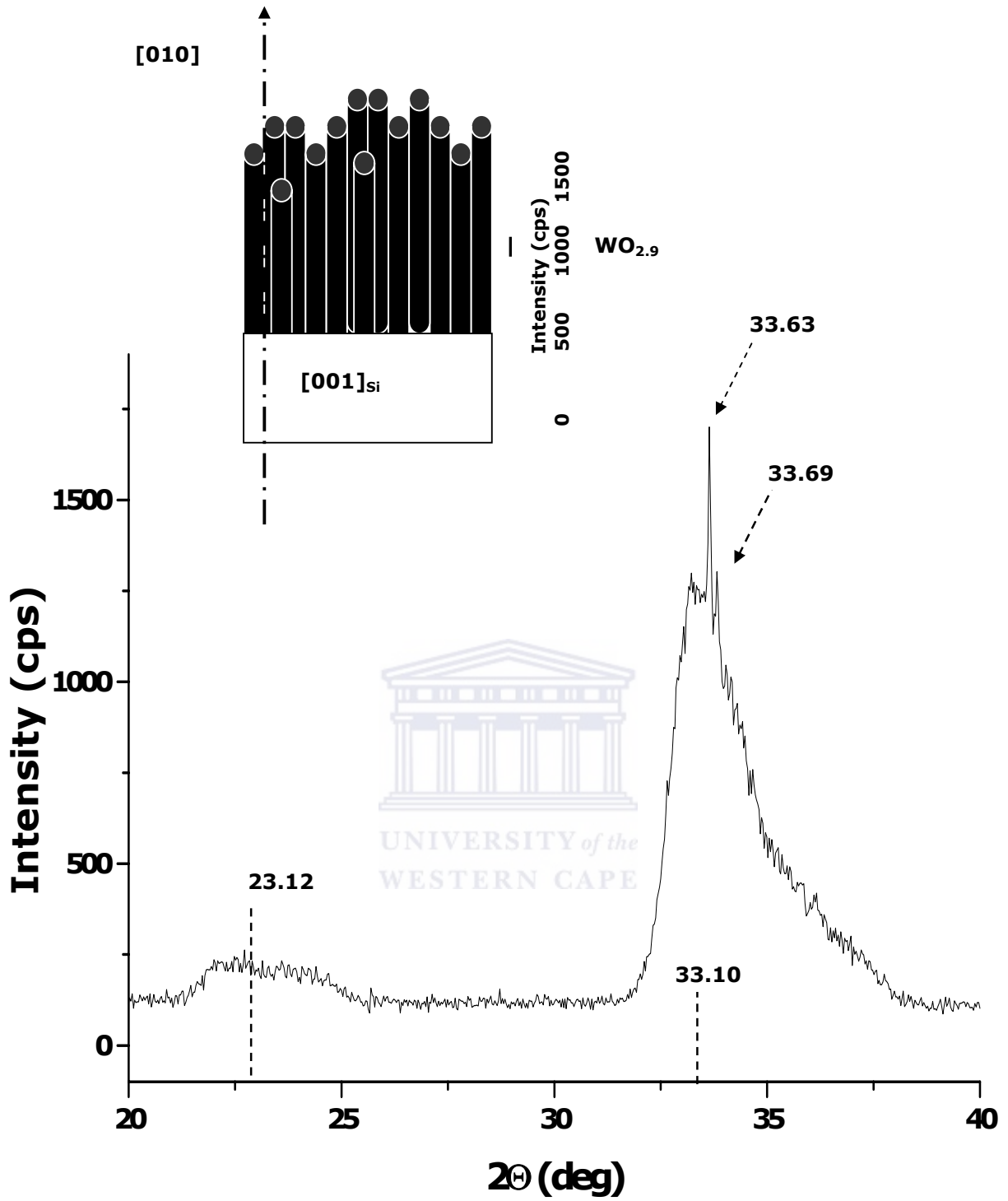


FIGURE 28

Texture and spatial orientation of the tungsten oxide nanorods deposited on Si(001) substrates.

6.6 Optical properties in UV-VIS-NIR spectral range

As the scope of this research project is to enhance the optical modulation and the reversible dynamic of tungsten oxide based electrochromic devices by using nanorod shape anisotropy of the tungsten oxide layer, one should ensure that the optical transmission of the nanorods coatings on the glass is comparable to the standard electrochromics. Hence, optical transmissions in the range of 200-900 nm were performed. These room temperature measurements were taken at normal incidence on a Perkin-Elmer Lambda 9 spectrophotometer. Figure 29 shows representative optical transmission versus wavelength of three different tungsten nanorods types deposited on ultra-sonicated corning glass at different currents 8, 10 and 13.5A. For low currents and/or short time of deposition as in (a) the transmission is close to standard continuous amorphous tungsten oxide coatings: the transmission in the VIS and NIR is about 70% with sharp UV cut-off at about 350 nm. In the case of higher currents and/or longer deposited nanorods as in (b) and (c) the transmission degrades severely in the VIS range ($\leq 40\%$) while still large in the NIR ($\geq 50\%$). This reproducible decrease in the VIS optical transmission in the case of large deposition's time and/or higher currents could be due to the non diffusive scattering or light trapping in the long tungsten nanorods and their bundles. From diffusive scattering, the tungsten nanorods might act as a very rough surface-like system.

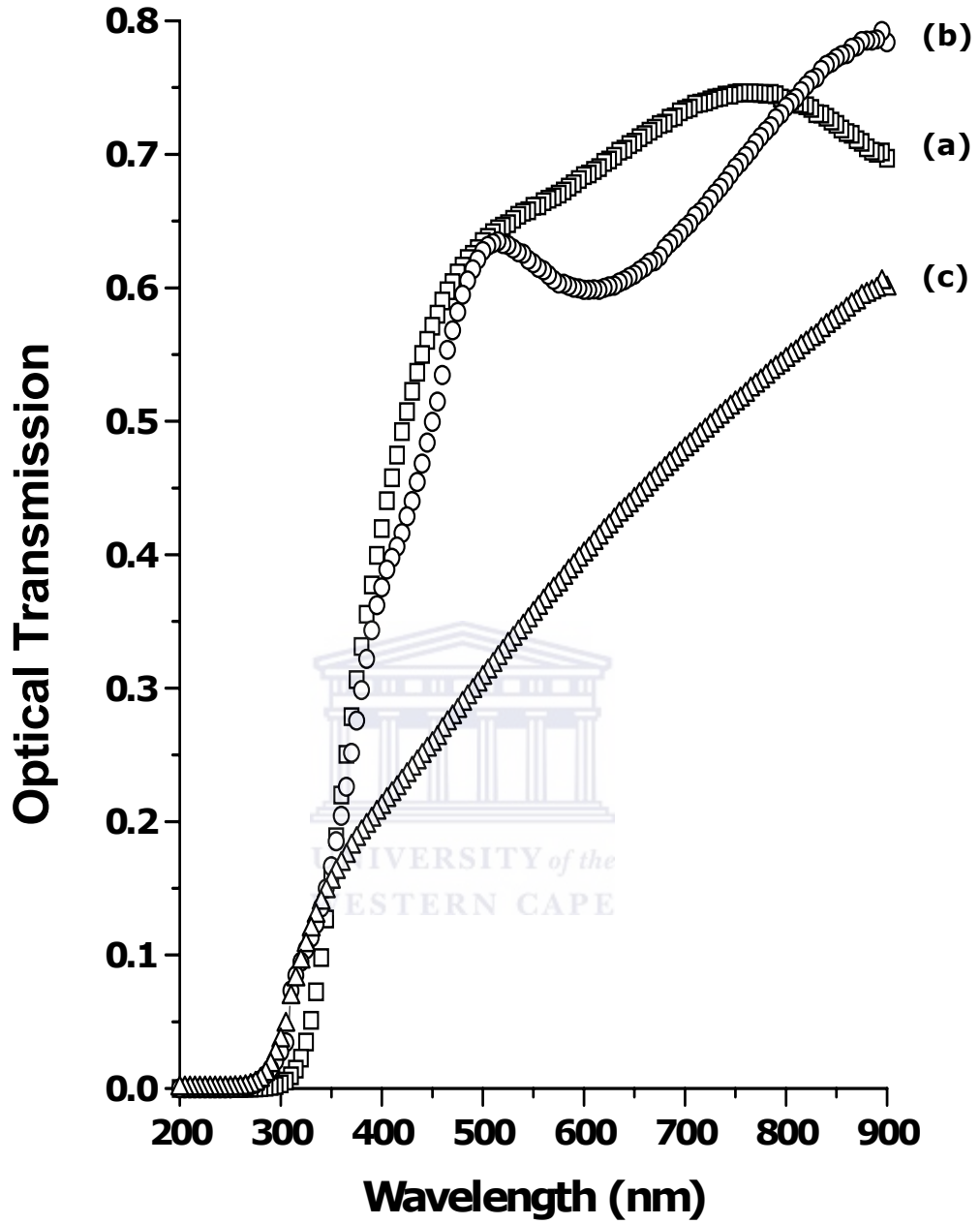


FIGURE 29

UV-VIS-NIR optical transmission of WO_{3-δ} nanorods coatings on corning glass substrates at different currents: (a) 8A, (b) 10A and (c) 13.5A.

CONCLUSIONS

The goal of this project was to prepare epitaxial well defined tungsten oxide nanorods by the thermal evaporation technique. After a series of samples were analyzed by high resolution electron microscopy, samples deposited on corning glass, Si and Mica showed some positive results, large area nanorods of WO_3 were synthesized and achieved through the thermal evaporation technique. The nanorods were successfully grown on corning glass and mica with a preferential spatial orientation parallel to the surface of mica and the glass. As one can see from the SEM micrographs, one deduces that the nanorods are larger both in transversal as well as in the longitudinal direction.

The tungsten nanorods grown on Si (001) are cylindrical in shape and display a columnar spatial orientation. The tungsten oxide nanorods deposited on mica and corning glass seem to grow parallel to the substrate for short depositions with exhibition of sharp edged crystallites. The density of these tungsten oxide nanorods is high in the case of Si(001) and low for mica and the corning glass.

In addition to the growth order, the nanorods presented quasi constant angles between them. RBS profile though difficult to obtained good simulations, has in fact been in agreement with previous studies that there is a significant shape anisotropy in the tungsten oxide system. The EELS investigations have shown homogeneity in the elemental distribution of W and O within the basal plane of the deposits.

The optical transmission results shows that nanorods deposited with higher currents, their transmission degrades in the VIS range while still large in the NIR.

There are some challenges remaining in the synthesis of WO_3 nanorods. In our opinion, synthesis of aligned WO_3 nanorods could provide a platform for better enhancement of the optical modulation and the reversible dynamic of tungsten oxide based electrochromic devices. Further refinements of the deposition conditions will improve the quality of the nanorods obtained, and highly oriented nanorods could be synthesized with ease



REFERENCES:

1. C.G Granqvist, Handbook of inorganic Electrochromic Materials, Elsevier, Amsterdam, (1995)
2. C.G Granqvist, M.H Francombe, J.L Vossen (Eds.), Physics of Thin Film, Academic, San Diego, **70**, 301-370 (1993)
3. C.G Granqvist, Solid State Ionics **60**, 213 (1993)
4. L. S. Wang, B.P. Hichwa, S.P. Sapers, N.A. O'Brien, in "Thin Film Solid State Ionic Devices and Materials", Proc. **95-22**, The Electrochem Soc., Pennington, 63 (1995)
5. S.K. Deb, Appl. Optics, Suppl. 3 on Electrophotography, 192-195 (1969)
6. J.G.H Mathew, S.P. Sapers, M.J. Cumbo, N.A. O'Brien, R.B. Sargent, V.P. Raksha, R.B. Lahaderne, B.P. Hichwa, J. Non-Cryst. Solids **218**, 342 (1997)
7. C. Bittencourt, R. Landers, E. Llobet, G. Molas, X. Correig, M.A.P. Silva, J.E Sueiras, J. Electrochemical Society, **149**, H81-H86 (2002).
8. C.G. Granqvist, A. Azens, J. Isidorsson, M. Kkarrazi, L. Kullman, T. Lindstrom, G.A. Niklasson, C.G. Ribbing, D. Ronnow, M.S. Mattsson, M. Veszeli, J. Non-Cryst. Solids **218**, 273 (1997)
9. S.K. Deb, Phil. Mag. **27**, 801(1973)
10. M. Green, S. K. Kang, Thin Solid Films **62**, 385 (1979)
11. B.W. Faughnan, R.S. Crandal, P.M. Heyman, RCA Review **36**,177 (1975)
12. O. Bohnke, PhD Thesis, Order number 181(France), (1984)
13. Magneli, A. Ark, Kemi. **1**, 513 (1950)
14. P. W Anderson, Phys. Rev. **109**, 1492 (1958)
15. P.M. Woodward, A.W. Sleight, T. Vogt, J. Phys. Chem. Solids **56**, 1305-1315 (1995)

16. Y. Xu, S. Carlson, R. Norrestam, *J.Sol.State Chem.* **132**, 132-130 (1997)
17. E. Cazzanelli, C. Vinegoni, G. Mariotto, A. Kuzmin, J. Purans, *J. Sol. State Chem.* **143**, 24 (1999)
18. E. Cazzanelli, C. Vinegoni, G. Mariotto, A. Kuzmin, J. Purans, *Proc. Electrochem. Soc.* **96-24**, 260 (1996)
19. R. Diehl, G. Brandt, E. Salje, *Acta Crystallogr. B* **34**, 1105 (1978)
20. E. Cazzanelli, C. Vinegoni, G. Mariotto, A. Kuzmin, J. Purans, *Sol. State Ionics* **123**, 67-74 (1999)
21. S. Tanisaki, *J. Phys. Soc. Jpn.* **15**, 573 -581(1960)
22. T Vogt, P.M Woodward, A.B Hunter, *J. Solid State Chem.* **144**, 209-215 (1999)
23. Gerand, B. Nowogrocki, G. Guenot, J. Figlarz, *M. J. Solid State Chem.* **29**, 429 (1979)
24. O. Glemser, H. Sauer, *Z. Anorg. Chem.***252**, 44-158 (1943)
25. A. Deneuveille, P. Gerard, *J. Elect. Mater.***7**, 559 (1978)
26. G.A. Niklasson, L. Bergren, A.L. Larson, *Solar Energy Matter and Solar Cells.* **84**, 315-328 (2004)
27. J. Ederth, A. Hoel, G.A Niklasson, C.G. Granqvist, *J. Appl. Phys.* **96**, 102 (2004)
28. Ch. J. Raub, A. R. Sweedler, M. A. Jensen, S. Broadston, B. T. Matthias, *Phys. Rev. Lett.* **13**, 746–747 (1964)
29. G. A de Wijs, P. K de Boer, R. A de Groot, G. Kresse, *Phys. Rev. B* **59**, 2684 (1999)
30. D.W Bullet , *J. Phys. C* **16**, 2197 (1983)
31. L. Kopp, B. N Harmon, S. H. Liu, *Solid State Commun.* **22**, 677 (1977)

32. G.Gu, B. Zheng, W.Q. Han, R. Siegmar, J. Liu, Nano Lett. **2**, 829 (2002)
33. J. Liu, Ye. Zhao, Z. Zhang, J. Phys.: Condens. Matter **15**, L453-L461 (2003)
34. M. Deepa, A.K. Srivastava, K. N. Sood, S.A. Agnihorty, Nanotechnology **17**, 2625 (2006)
35. C.H. Chen, S.J. Wang, R.M Ko, Y.C. Kuo, K.M. Unag, T. M. Chen, B.W. Liou, H. Y. Tsai, Nanotechnology **17**, 217 (2006)
36. C.C. Liao, F.R. Chen, J.J. Kai, Solar Energy Mater. and Solar Cells, **90**, 1147 (2006)
37. C.C. Liao, F.R. Chen, J.J. Kai, Solar Energy Materials and Solar Cells, **90**, N° 7 - 8, 1147 (2006)
38. M. Gillet, R. Delamare, E. Gillet, Eur. Phys. J. **D34**, 291 (2005)
39. Wagner R. S, Ellis W C App. Phys. Lett. **4**, 89-90 (1964)
40. www.webelements.com
41. M. Figlarz, J. Solid State Chem. **67**, 235 (1987)
42. R. Fan, X.H. Chen, Z. Gui, Z.Y. Chen, J. Phys. Chem. Sol.**61**, 2029 (2000)
43. X.G. Yang, C. Li, M.S. Mo, Y.T. Qian, J. Cryst. Growth **249**, 594 (2003)
44. Whisker Technology Wiley Interscience, New York, 257 (1970)
45. J.M. Norras, M.D. Ryall, J. Phys. D.: Appl. Phys.**12**, 277 (1979)
46. K R Locherer *et al* 1999 *J. Phys.: Condens. Matter* **11** 4143-4156